Journal of Materials Chemistry A

ROYAL SOCIETY OF CHEMISTRY

PAPER

View Article Online
View Journal | View Issue

Cite this: *J. Mater. Chem. A*, 2020, **8**, 3803

Fabrication of a freestanding metal organic framework predominant hollow fiber mat and its potential applications in gas separation and catalysis†

Zijian Dai, [ab] Dennis T. Lee, [b] Kaihang Shi,[b] Siyao Wang,[b] Heather F. Barton,[b] Jie Zhu,[c] Jiaqi Yan, [b] Qinfei Ke*[a] and Gregory N. Parsons *[b]

Received 24th October 2019
Accepted 23rd January 2020

DOI: 10.1039/c9ta11701f

rsc.li/materials-a

Recently, metal–organic framework (MOF)-based polymeric substrates show promising performance in many engineering and technology fields. However, a commonly known drawback of MOF/polymer composites is MOF crystal encapsulation and reduced surface area. This work reports a facile and gentle strategy to produce self-supported MOF predominant hollow fiber mats. A wide range of hollow MOFs including MIL-53(Al)–NH_2, Al-PMOF, and ZIF-8 are successfully fabricated by our synthetic method. The synthetic strategy combines atomic layer deposition (ALD) of metal oxides onto polymer fibers and subsequent selective removal of polymer components followed by conversion of remaining hollow metal oxides into freestanding MOF predominant hollow fiber structures. The hollow MOFs show boosted surface area, superb porosity, and excellent pore accessibility, and exhibit a significantly improved performance in CO_2 adsorption (3.30 mmol g^{-1}), CO_2/N_2 separation selectivity (24.9 and 21.2 for 15/85 and 50/50 CO_2/N_2 mixtures), and catalytic removal of HCHO (complete oxidation of 150 ppm within 60 min).

Introduction

Metal–organic-frameworks (MOFs) are highly crystalline and porous materials consisting of metal ions or clusters which are coordinated with organic linkers.[1,2] Impressive progress has been made using MOFs in gas storage and separation,[3,4] volatile organic compound (VOC) adsorption,[5–7] heterogeneous catalysis,[8–15] and environmental decontamination.[16] These advances result from the unique advantages of MOFs, such as controllable pore size, high surface areas and porosity, well-dispersed active centers, and tailorable functionalities.

Because MOF powders are difficult to handle and utilize,[17] significant research effort is focused on integrating MOFs into robust MOF-fibers,[18,19] and membranes.[20,21] A polymer fiber or membrane provides mechanical support and can substantially reduce MOF aggregation, leading to improvement in functional performance on a per-gram of MOF basis. MOF/fiber composites have shown marked advantages in catalysis,[22] pollution control,[23] gas separation,[24] and sensing[25] applications. Moreover, MOF/fiber composites enable more than one type of MOF to be coupled together to simultaneously perform multiple functions.[19]

Despite the reported advances in MOF polymer composites, there are several common challenges to create high performance structures. For example, during formation, the polymer from the fiber can infuse or otherwise unfavorably interact with the MOF to block pore access.[26] Also, for biomedical applications, biocompatible polymers (*e.g.*, polyvinylpyrrolidone, polyvinylalcohol, poly(lactic-*co*-glycolic acid), and gelatin)[27] must be used to construct the MOF polymer composites, thereby limiting the substrate selection.

While several groups have demonstrated MOF/fiber composites, very few reports describe approaches to produce free-standing MOF fiber mats or provide quantified functional performance of the products. Li and coauthors reported a strategy applying soft ceramic oxide fibers as MOF conversion templates, and suggested that resulting MOF fibers would retain the original fiber flexibility and softness.[26,28] Dwyer *et al.* demonstrated a unique synthetic approach to create hollow TiO_2 cylinders with dense MOF crystals on the inner and outer surfaces.[29] These methods possess some drawbacks such as low

[a]*Key Laboratory of Textile Science & Technology, Ministry of Education, College of Textiles, Donghua University, Shanghai, 201620, China. E-mail: kqf@sit.edu.cn*

[b]*Department of Chemical & Biomolecular Engineering, North Carolina State University, 911 Partners Way, Raleigh, North Carolina 27695, USA. E-mail: gnp@ncsu.edu*

[c]*School of Fashion Engineering, Shanghai University of Engineering Science, No. 333 Longteng Road, Songjiang, Shanghai, 201620, China*

† Electronic supplementary information (ESI) available: Detailed experimental procedures; additional information pertaining to SEM and XRD; MOF conversation ratio results; low temperature gas adsorption results; isotherms from IAST simulations; CO_2/N_2 selectivity results (PDF). See DOI: 10.1039/c9ta11701f

surface area, and time- and energy-consuming material processing.

Here, we report a facile and unique approach to synthesize freestanding MOF enriched hollow structures *via* oxide-to-MOF conversion, also known as coordination replication.[30,31] The metal oxides used here, Al_2O_3 and ZnO, are formed conformally on starting polymer fibers using low-temperature atomic layer deposition (ALD).[18,19,22,32] These oxides allow successful synthesis of MIL-53(Al)–NH_2, Al-PMOF, and ZIF-8 MOFs. In this work, cellulose diacetate (CDA), a cost-effective polymer that readily dissolves in acetone or DMF, was selected as the sacrificial polymer for freestanding MOF fabrication. First, a stable metal oxide layer is formed on the fiber surface by ALD, and then the polymer is selectively dissolved in acetone solution leaving only the metal oxide hollow structure. The oxide tube is then converted to a hollow MOF by reacting with organic linkers. The process yields hollow fibers with a small (~500 nm) diameter suitable for filtration structure, but size and mechanical handling inhibit testing as hollow fiber separator systems. This work further describes the versatility and performance of the freestanding MIL-53(Al)–NH_2 predominant hollow fiber mats as filters for CO_2 adsorption, CO_2/N_2 separation, and VOC removal. This work is the first to report synthesis of a freestanding MOF fiber with the feature of a hollow structure, and it directly demonstrates a novel and unique approach to MOF crystal size and pore configuration control which is a common challenge in MOF powder growth. In addition, this study highlights the importance of MOFs in gas separation and VOC heterogeneous catalysis, and may contribute to the design of high-performance adsorbents.

Experimental

Materials

Electrospinning polymer: cellulose diacetate (CDA, Eastman Chemicals); *ALD precursors*: diethyl zinc (DEZ, 95% STREM Chemicals Inc.,) and trimethyl aluminum (TMA, 98% STREM Chemicals Inc.,); *metal sources*: aluminum chloride hexahydrate ($AlCl_3 \cdot 6H_2O$, Alfa Aesar) and copper nitrate trihydrate ($Cu(NO_3)_2 \cdot 3H_2O$, 99–104%, Sigma-Aldrich); *linkers*: 2-aminoterephthalic acid (99%, Acros Organics), 2-methylimidazole (99%, Sigma-Aldrich), and *meso*-tetra(4-carboxyphenyl) porphine (H_2TCPP, >97% Frontier Scientific); *organic solvents*: acetone (Fisher), *N*,*N*-dimethylformamide (DMF, Fisher), *N*,*N*-dimethylacetamide (DMAc, 99.8%, Sigma-Aldrich), and anhydrous ethanol (200 proof, VWR) were purchased from commercial sources and used without further treatment. Melt-blown polypropylene (PP) fiber mats with a density of 40 gsm were used as received from the Nonwovens Cooperative Research Center (NCRC), North Carolina State University.

Synthesis of MIL-53(Al)–NH_2 predominant hollow fiber mats

To synthesize MIL-53(Al)–NH_2 predominant hollow fiber mats, the Al_2O_3 ALD coated CDA nanofiber mats (denoted as Al_2O_3@CDA) were first immersed in acetone and heated up to 120 °C for 24 h in a sealed Teflon-lined stainless-steel autoclave reactor to dissolve and remove the CDA polymers. After the heat treatment in acetone, the majority of CDA polymers (~90%) were removed from the Al_2O_3@CDA nanofiber mats, which can be calculated by the mass change before and after acetone treatment, leaving the Al_2O_3 hollow fiber mats with tiny polymer residuals. For the conversion of MIL-53(Al)–NH_2 using Al_2O_3 hollow fiber mats as the metal source, 0.106 g 2-aminoterephthalic acid was firstly added to a 20 mL DMF/water mixture (3/1, v/v), and then the mixture was sonicated and stirred for 20 min until complete dissolution. Subsequently, a piece of Al_2O_3 hollow fiber mat (0.030 g) was gently soaked in the prepared solution and transferred into a 100 mL Teflon-lined stainless-steel autoclave reactor. This reactor was then heated at 120 °C for 20 h to finish the solvothermal synthesis. After reaction completed, the as-received MIL-53(Al)–NH_2 hollow fiber mat was washed twice with hot DMF, followed by another 2 times of anhydrous ethanol washing. The MIL-53(Al)–NH_2 hollow fiber mat was finally dried under vacuum at 200 °C for 10 h and stored in a desiccator before test. As a control group, the Al_2O_3@CDA nanofiber mat was also converted into MIL-53(Al)–NH_2 directly using the same recipe mentioned above without the pretreatment in acetone solution. The as-prepared sample was denoted as MIL-53(Al)–NH_2 (CDA).

Characterization

Scanning electron microscopy (SEM) was conducted using a FEI Verios 460 L field emission SEM. X-ray diffraction (XRD) data were collected using a Rigaku SmartLab X-ray diffraction tool (Cu Kα X-ray source) for crystalline structure characterization. X-ray photoelectron spectroscopy (XPS) was performed using a Kratos Analytical Axis Ultra system equipped with an aluminum source (Al Kα = 1486.6 eV radiation). The voltage and current of the X-ray gun were 15 kV and 20 mA. All the binding energies were calibrated using the signal from adventitious carbon (C 1s = 284.6 eV). *In situ* diffuse reflectance infrared Fourier transform spectrometry (DRIFTS) was performed on a Fourier transform infrared (FTIR) spectrometer (Model Nicolet 6700, Thermo Fisher, USA). The spectra were recorded with a resolution of 4 cm^{-1} and an accumulation of 64 scans. During the HCHO oxidation process, ~80 ppm of HCHO was injected into the DRIFTS cell carried by a synergetic gas (80% N_2, 20% O_2) at a flow rate of 30 mL min^{-1} at room temperature.

Low-pressure gas adsorption measurements

Gas adsorption isotherms in the pressure range of 0–1.1 bar were measured by a volumetric method using a Micromeritics 3Flex Surface Characterization Analyzer. Before analysis, all samples were fully degassed under vacuum at 120 °C for 20 h by using the Smart Vacprep (Micromeritics), a gas adsorption sample preparation device. After the degassing process was completed, the sample tubes were weighed and then carefully transferred to the analysis port of the gas adsorption instrument. N_2 adsorption–desorption isotherms at 77 K were measured in liquid nitrogen. N_2 and CO_2 adsorption–desorption isotherms at 273 K were measured using an ice water bath and isotherms at 298 K were measured using water baths. All

temperatures were monitored before and after the measurement and no temperature change was detected in all cases.

Thermogravimetric analysis and CO_2 cycling measurement

CO_2 cycling experiments were carried out on a TA instruments SDT 650. 15% CO_2/N_2 (Acro) and N_2 (99.999%) were used in this experiment. In a typical test, ~10 mg of the target sample was loaded into an alumina pan, with a flow rate of 100 mL min^{-1} for both gases. The sample was first heated at 100 °C for 40 min under a N_2 atmosphere to complete degassing, and after the temperature was cooled to 25 °C, the MOF sample was swept continuously with CO_2 for 20 min, and then flowing N_2 was maintained for 40 min at 100 °C to activate the MOF sample in every cycle. All ramp rates were set as 10 °C min^{-1}.

Adsorption and catalytic activity test

The HCHO adsorption and catalytic activities were evaluated in the static state using reported procedures.[33] Specifically, a polytetrafluoroethylene layer stainless steel reactor (0.5 L) was used, at the bottom of which was placed a quartz Petri dish which held the material under test. After putting the dish into the reactor, 300 ppm of HCHO, generated using an S-4000 Gas Mixing system (Environics, USA), was injected into the reactor. After the concentration of HCHO was stabilized to 150 ppm, the cover of the dish was removed to start the adsorption and catalytic reaction of HCHO. HCHO, CO_2, CO and water vapor were recorded online by a photoacoustic IR multigas monitor (INNOVA AirTech Instruments Model 1412i) during the test at 25 °C. The yield of CO_2 (ΔCO_2) and the concentration variation of HCHO were calculated to analyze the HCHO removal ratio.

Results and discussion

Synthesis and characterization of MIL-53(Al)–NH_2 hollow fiber mats

The procedure developed here for synthesizing freestanding hollow MOFs is shown in Scheme 1. Using MIL-53(Al)–NH_2 as an example, the first step was the electrospinning of a CDA nanofiber mat with a fiber diameter in the range of 300–500 nm. The as-prepared CDA nanofiber mat was transferred to a lab-made ALD reactor and coated with a conformal metal oxide layer to construct a core–sheath structure. This Al_2O_3 ALD layer functions as a metal source for MOF structure synthesis by reacting with organic linkers. For most experiments, before MOF synthesis, the Al_2O_3@CDA mat was immersed in acetone at 120 °C for 12 h to dissolve the CDA, yielding an Al_2O_3 hollow fiber mat (Fig. S1 and S2†). Then, the hollow Al_2O_3 structure was transferred into the solution containing the 2-amino-terephthalic acid linker dissolved in the water/DMF mixed solvent and heated to 120 °C for 20 h. Using this solvothermal synthesis method, the Al_2O_3 hollow structure transformed into MIL-53(Al)–NH_2 and the initial hollow structure remained intact (Fig. 1A and B).

Scanning electron microscopic (SEM) imaging and X-ray diffraction (XRD) confirmed successful formation of MIL-53(Al)–NH_2 hollow fiber mats. As shown in Fig. 1B, a rod-like morphology was observed for hollow MIL-53(Al)–NH_2. The MOF crystals with the average size of around 200 nm length and 5 nm diameter were conformally formed along the surface of the fiber cylinders. In Fig. 1C, the observed characteristic peaks resemble those expected for the MOF with large pore (lp) configuration although the narrow pore (np) structure has been obtained previously for the MIL-53(Al)–NH_2 powder.[34,35]

To obtain the highest quality of hollow MOF fiber mats, systematic experiments were conducted by tuning the thickness of the Al_2O_3 ALD layer. Using 100, 200, and 300 cycles of ALD treatment, that thickness ranges from 12 nm to 40 nm (Table S1 and Fig. S3†), denoted as MIL-53(Al)–NH_2 (100), MIL-53(Al)–NH_2 (200), and MIL-53(Al)–NH_2 (300), respectively. By analyzing the results from SEM, XRD, N_2 isotherms, and XPS we found around the 200 cycle sample with a thickness of 28 nm was optimal to transform into a high quality MOF. As shown in Fig. 1D–F, MIL-53(Al)–NH_2 (100), MIL-53(Al)–NH_2 (200), and MIL-53(Al)–NH_2 (300) exhibit similar morphologies. Moreover, thicker ALD layers tend to produce MOFs with a larger crystal size. XRD patterns of the samples prove that there is a slight loss in crystallinity with the increase of the ALD layer thickness (Fig. 1G). In addition, XRD patterns corresponding to the lp configuration were observed in all MOFs.

A high surface area was calculated from N_2 adsorption isotherms at 77 K for the hollow MOF-fibers and the relation between the MOF surface area and the starting thickness of ALD Al_2O_3 was elucidated. For all hollow MIL-53(Al)–NH_2 fibers, the N_2 adsorption–desorption isotherms at 77 K exhibit slight hysteresis (at higher pressure, P/P_0 > 0.4) (Fig. 1H) reflecting

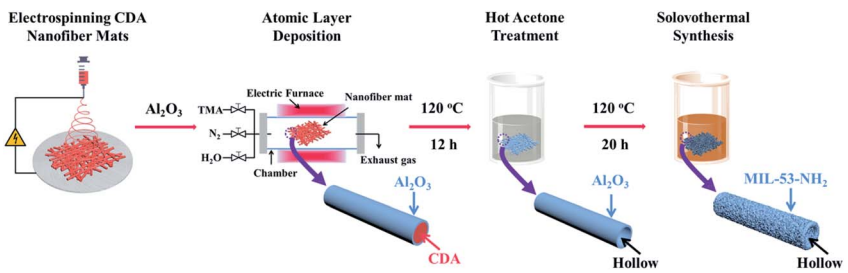

Scheme 1 Schematic illustration of the fabrication of the hollow MIL-53(Al)–NH_2 fiber mat. The Al_2O_3 hollow fiber mat (obtained from dissolving Al_2O_3@CDA into acetone) was employed as the metal source, and was then transferred into the water/DMF mixed solution containing the 2-amino-terephthalic acid linker, which was heated to 120 °C for 20 h.

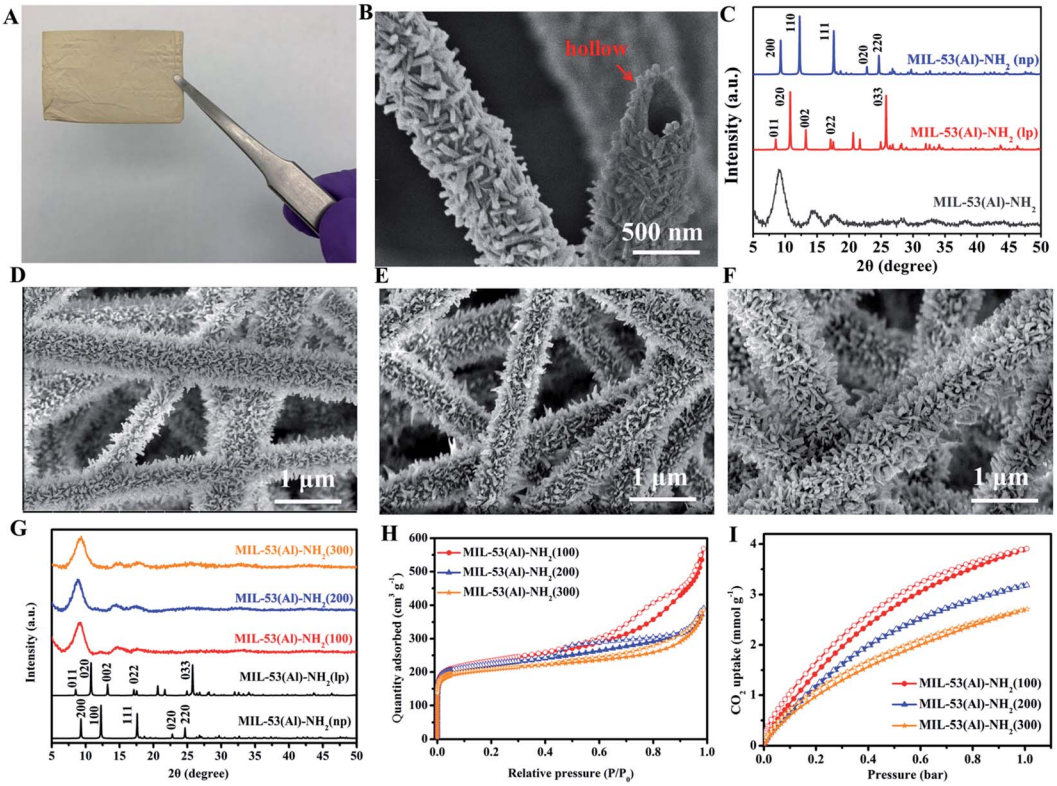

Fig. 1 (A) Optical photograph of the freestanding hollow MIL-53(Al)–NH_2. (B) Cross-sectional SEM image of the hollow MIL-53(Al)–NH_2 fiber mat. (C) XRD pattern of the MIL-53(Al)–NH_2 fiber mat with the simulated patterns for the lp and np configurations of MIL-53(Al)–NH_2.[36] SEM images of the (D) MIL-53(Al)–NH_2 (100), (E) MIL-53(Al)–NH_2 (200) and (F) MIL-53(Al)–NH_2 (300). Rod-like crystals are observed in all cases, and as the ALD layers get thicker, the obtained MOF crystal sizes increase. (G) XRD pattern of the hollow MIL-53(Al)–NH_2 fiber mat fabricated with different ALD thicknesses. All XRD patterns reveal an lp configuration. (H) N_2 isotherms at 77 K. (I) CO_2 isotherms at 273 K.

a hierarchical pore structure, involving micro, meso- and macro-porosity. The MIL-53(Al)–NH_2 crystals contribute to the microporous structure, whereas the spaces between these crystals, hollowness of the fibers, and fibrous mats give rise to meso- and macro-porosity.[22] These meso–macro-porosities with complex pore geometry are consistent with the observed hysteresis in the isotherms, and may lead to capillary condensation at high relative pressure.[37,38] As shown in Fig. 1H, the Brunauer–Emmett–Teller (BET) surface area of MIL-53(Al)–NH_2 (100), MIL-53(Al)–NH_2 (200), and MIL-53(Al)–NH_2 (300) is 880 ± 30 $m^2\ g^{-1}$, 842 ± 28 $m^2\ g^{-1}$, and 720 ± 40 $m^2\ g^{-1}$, respectively. The resulting DFT pore diameter distribution curves (Fig. S4†) show that the pore size of all MIL-53(Al)–NH_2 fiber mats is predominantly microporous (0.5–2 nm).[39–41] The textural parameters derived from the N_2 isotherms are included in Table S1.†

CO_2 isotherms at 273 K in Fig. 1I display the same trend of decreasing adsorption capacity on a per-gram basis for hollow MIL-53(Al)–NH_2 materials synthesized with thicker Al_2O_3 layers. Notably, all CO_2 adsorption capacities at 273 K are improved compared to those of MIL-53(Al)–NH_2 powder samples reported,[42,43] due to the more stable lp configuration, indicating the great potential of our materials in CO_2 capture or other gas separations.

Analysis of MOF conversion yield

Mass measurements were used to examine MOF quality. The MOF conversion yield was calculated using measured mass, following a procedure adapted from previous reports,[44] and the results are given in Table S1.† The yield values given in Table S1† reveal 100% conversion for the thinnest Al_2O_3 layer, with somewhat decreased yield for thicker oxides.

X-ray photoelectron spectroscopy (XPS) analysis was also used to qualitatively confirm the elemental composition of the MOFs. As illustrated in Fig. 2, the XPS data reflected a similar trend to the mathematical calculation. Two peaks are detected at the Al 2p high resolution scan of MIL-53(Al)–NH_2 (300) (Fig. 2A), where the component at 74.50 eV corresponds to octahedral $AlO_4(OH)_2$ clusters in MOFs, and the component at 75.35 eV is attributed to the unreacted aluminum oxide or byproducts of hydroxide in the hollow structure.[45]

Notably, when thinner Al_2O_3 layers are used, the peak areas for unreacted aluminum oxide at 75.4 eV decrease significantly and no peak is detected for MIL-53(Al)–NH_2 (100) (Fig. 2G). As observed in the yield calculation, the XPS result also denotes 100% conversion into MIL-53(Al)–NH_2 from the Al_2O_3 film with 12 nm thickness. In addition, the O 1s spectra can be divided into two peaks. As shown in Fig. 2B, E and H, the first peak at 531.5 eV is attributed to the coordination of the Al cations with the oxygen

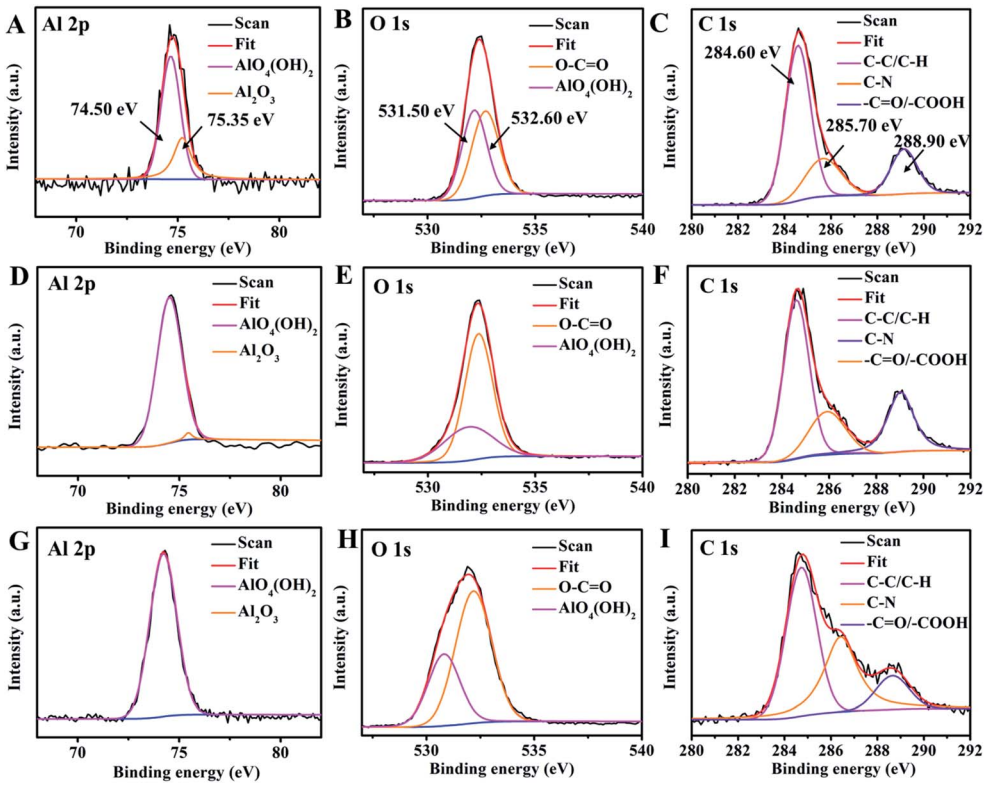

Fig. 2 High resolution XPS scans of (A) Al 2p (B) O 1s and (C) C 1s for MIL-53(Al)–NH_2 (300). (D) Al 2p (E) O 1s and (F) C 1s for MIL-53(Al)–NH_2 (200). (G) Al 2p (H) O 1s and (I) C 1s for MIL-53(Al)–NH_2 (100).

anion of the 2-amino-terephthalic acid linker, whereas the latter one at 532.6 eV is assigned to the oxygen in O–C=O. There are three peaks in C 1s emission spectra (Fig. 2C, F and I), which can be assigned to the non-oxygenated ring carbon (284.6 eV), C–N bond (285.7 eV), and carboxylate carbon (288.6 eV), respectively.

As shown in Fig. S5,† MIL-53(Al)–NH_2 (200) and MIL-53(Al)–NH_2 (300) form as robust mats, whereas MIL-53(Al)–NH_2 (100) is evidently fragile due to the ultrathin Al_2O_3 shell. In view of structure robustness and MOF quality, MIL-53(Al)–NH_2 (200) was chosen for the application tests. With this information in mind, 200 cycles of ALD Al_2O_3 (*i.e.* a thickness of 28 nm) are fixed to provide the consumptive metal oxide source in the following experiments.

Growth mechanism

The mechanism for MOF syntheses from Al_2O_3 proceeds *via* a dissolution–growth process.[30,46] In detail, the reaction originates from fast dissolution and hydration of the surface oxide in DMF:water cosolvent; Al^{3+} species are then generated by the reaction between hydroxylated aluminum and adsorbed H^+ in the near-surface region yielding an aluminum aqua complex ($[Al(H_2O)_6]^{3+}$). Finally, MOF nucleation is promoted by the coordination between the aluminum aqua complex and the linkers.[46] However, as the MOF crystal growth consumes the outer Al_2O_3 layer, MOF crystals on the fiber surface can inhibit ligand diffusion into the inner region of the oxide layer,[30] thereby limiting MOF growth.[47,48]

Comparison to powders and extension to other fiber substrates

We further studied MIL-53(Al)–NH_2 powders produced *via* solvothermal synthesis (denoted as MIL-53(Al)–NH_2 (powder)), as well as MOF-fibers formed *via* oxide conversion on CDA and PP fibers (Materials and Synthesis ESI†). The latter materials are referred to as MIL-53(Al)–NH_2 (CDA) and MIL-53(Al)–NH_2 (PP), respectively. In these cases, the polymer was not removed before oxide-to-MOF conversion. Results of these materials, and comparison to MIL-53(Al)–NH_2 (200) fibers produced with the pre-dissolved polymer are shown in Fig. 3.

As shown in Fig. 3A, MIL-53(Al)–NH_2 powder samples produced rice-shaped crystals with crystal size in the range of 500–700 nm length and 80–150 nm diameter (Fig. 3A). For the case of MIL-53(Al)–NH_2 (CDA), the SEM image (Fig. 3B) shows a predominantly hollow MOF structure indicating that the CDA polymer scaffold was dissolved during the MOF synthesis. For MIL-53(Al)–NH_2 (PP), the polymer was not dissolved, yielding a conformally integrated MOF on PP fibers, as shown in Fig. 3C.

It is also important to note that in contrast to the relatively large MIL-53(Al)–NH_2 crystals produced as powders, the crystals converted from ALD Al_2O_3 on fibers (Fig. 3B and C) are more well defined and smaller, less than 250 nm in length, which was consistent with the proposed growth mechanism. For all cases, the XRD patterns (Fig. 3D) of MIL-53(Al)–NH_2 (powder), MIL-53(Al)–NH_2 (CDA), and MIL-53(Al)–NH_2 (PP) show the characteristic peaks, indicating the successful MOF synthesis. The

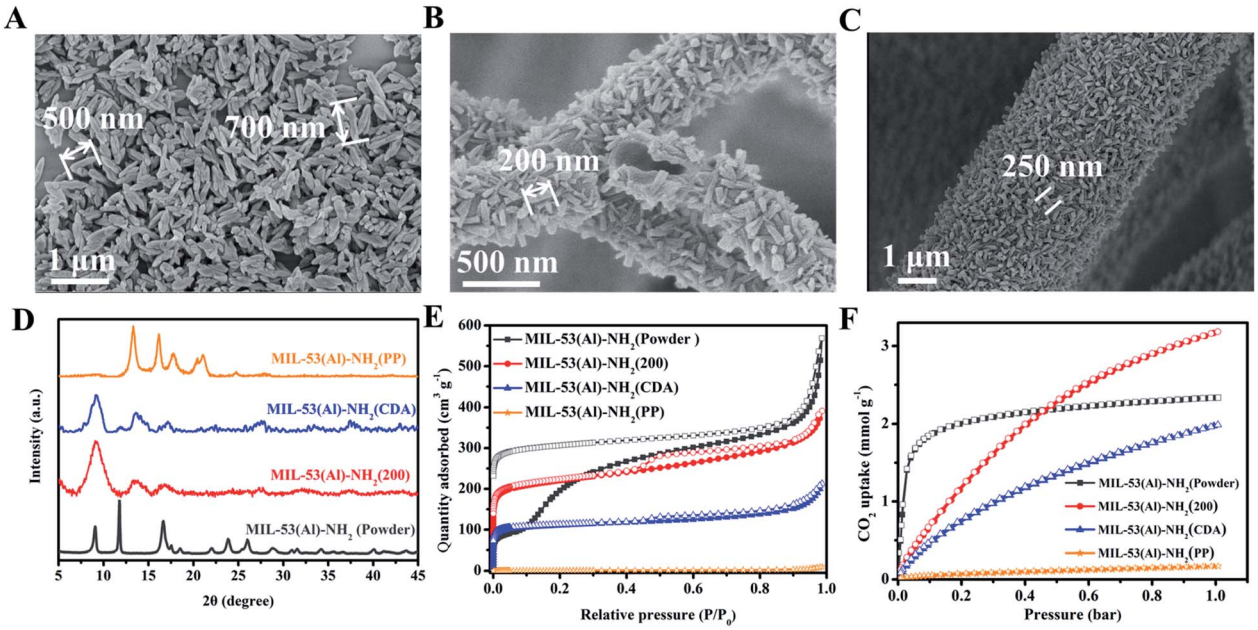

Fig. 3 SEM images of the (A) MIL-53(Al)–NH_2 (powder), (B) MIL-53(Al)–NH_2 (CDA) and (C) MIL-53(Al)–NH_2 (PP). MIL-53(Al)–NH_2 converted from the metal oxide source given by an ALD process shows a reduced crystal size (D) XRD patterns of MIL-53(Al)–NH_2 materials fabricated by different methods. MIL-53(Al)–NH_2 (200), MIL-53(Al)–NH_2 (CDA) and MIL-53(Al)–NH_2 (PP) can be assigned to the lp configuration, whereas MIL-53(Al)–NH_2 (powder) is much closer to the np configuration. (E) N_2 isotherms at 77 K. (F) CO_2 isotherms at 273 K.

powder samples show features consistent with the np structure, whereas like the materials shown in Fig. 1C, the MOF-fibers show spectra consistent with the lp configuration. The structural changes detected by XRD analysis show flexibility and breathing behavior in the MOFs. The flexibility is expected to arise from the parallel arrangement of the $Al^{III}(OH)(RCOO)_2$ chains and possibly some interpenetrated coordination.[49,50] This distinction is important as it influences the performance of the MOF-fibers relative to the free MOF powder.

Low-pressure gas adsorption analysis

MIL-53(Al)–NH_2 is known to be flexible with breathing behavior associated with lp–np transitions even at room temperature. The breathing behavior of MIL-53(Al)–NH_2 powders can be triggered by various gases such as CO_2, CH_4, and C_2H_6.[51] Kitagawa and co-workers described a close relationship between the MOF crystal size and the framework flexibility; that is, nanometer-scale crystals provide stability to the pore configuration in a flexible MOF structure, resulting in a thermodynamic and/or kinetic suppression in pore transitions.[25,52] Therefore, the smaller 200 nm lp dominated MIL-53(Al)–NH_2 (200) MOFs are expected to possess a much more stable pore configuration and be restricted further from breathing.

N_2 adsorption–desorption isotherms (Fig. 3E) confirm the hypothesis that MIL-53(Al)–NH_2 (200) features a much more stable pore structure than the powder phase. For MIL-53(Al)–NH_2 (powder), it shows an np configuration at room temperature, and the np–lp transition is evidently triggered at 120 °C by the degassing process.[53,54] In Fig. 3E, the N_2 adsorption isotherm at 77 K for MIL-53(Al)–NH_2 (powder) shows two plateaus, one at around 0.02–0.1 P/P_0 associated with the lp–np transition, and another at 0.4–0.6 P/P_0 associated with the np–lp transition.[55,56]

In separate tests, hollow MOF-fibers were produced from Al_2O_3 ALD layers either before or after removing the CDA fiber substrate. Removing the polymer before oxide-to-MOF conversion led to N_2 isotherms with a much more stable pore configuration and BET surface area of 842 ± 28 $m^2\ g^{-1}$. This surface area is ~2× larger than 480 ± 21 $m^2\ g^{-1}$ measured for MIL-53(Al)–NH_2 formed with the CDA not removed before oxide to MOF conversion. The small surface area for MOFs formed before polymer removal is ascribed to infusion of dissolved CDA into the MOF to partly block the pore volume (Table S1†). This highlights the significance of the pre-dissolution treatment in formation of a hollow structure MOF with fewer impurities and higher crystallinity. The pore size distribution results indicate that the MIL-53(Al)–NH_2 powder and MIL-53(Al)–NH_2–PP fiber show a hierarchical pore structure, whereas the MIL-53(Al)–NH_2 (CDA) fiber only shows a microporous structure (Fig. S6†).[39–41]

From the CO_2 isotherms, it can be observed that MIL-53(Al)–NH_2 (200) spans a higher range at a relative pressure at 0.4 bar over MIL-53(Al)–NH_2 (powder) isotherms, exhibiting a more stable pore configuration and higher CO_2 uptake (Fig. 3F). That is because, after the lp–np transition at 0–0.1 bar, MIL-53(Al)–NH_2 (powder) still forms in the np phase, and is unable to have additional gas uptake. In comparison, MIL-53(Al)–NH_2 (200) is stabilized in the lp phase and has continued adsorption throughout this region.[53,54]

Furthermore, among the four samples studied, MIL-53(Al)–NH_2 (200) shows the highest CO_2 uptake at 1 bar, reaching 3.30

$\pm$ 0.05 mmol g^{-1} (Table S1†) which is significantly higher than those reported in previous studies.[42,57]

Extension to other MOF materials

To confirm that our synthetic approach can be extended to other materials, we synthesized other hollow MOF fibers including Zn and Al based structures (Methods, ESI†). Fig. 4 shows Al-PMOF and ZIF-8 structures formed by transformation from the Al_2O_3 hollow structure, yielding freestanding MOF predominant nanofiber mats. The SEM images, XRD patterns, and N_2 adsorption–desorption isotherms (Fig. 4) confirm successful fabrication of the MOF structure.

Potential applications on MIL-53(Al)–NH_2 hollow fiber mats

The performances of the MIL-53(Al)–NH_2 fiber mats and powders were evaluated in gas separation and VOC removal applications. Over the past decade, experimental and computational analyses show promising potential for MOFs in CO_2 capture[58–60] and CO_2/N_2 and CO_2/CH_4 separation.[49,61,62] For the MIL-53(Al)–NH_2 hollow fiber samples produced here, volumetric gas adsorption analysis shown in Fig. 3F confirms high CO_2 adsorption capacities, showing promise for advanced applications.

To analyze CO_2/N_2 selectivity, we applied the ideal adsorbed solution theory (IAST) using adsorption data of single-component gases (Table S2 and Fig. S7–S10†).[63–68] As shown in Fig. 5, the MIL-53(Al)–NH_2 (200) material shows a moderate CO_2/N_2 selectivity. The values of IAST selectivity at 273 K and 1 bar for 15/85 and 50/50 CO_2/N_2 mixtures are about 24.9 and 21.2, respectively. It should be pointed out that MIL-53(Al)–NH_2 (200) shows much lower selectivity compared with MIL-53(Al)–NH_2 (powder) (Fig. S11†). We attribute this to the inherent low N_2 uptake on the powder, which results in ultrahigh CO_2/N_2 selectivity on MIL-53(Al)–NH_2 (powder) both in 15/85 and 50/50 CO_2/N_2 mixtures at 1 bar.

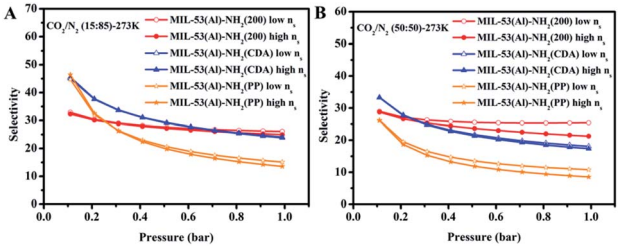

Fig. 5 Selectivity by the IAST calculations at 273 K with CO_2 and N_2 molar ratios of (A) 15/85 and (B) 50/50 in the gas phase.

The CO_2/N_2 selectivity is further confirmed by a binary gas-adsorption experiment *via* a gravimetric method, where the CO_2/N_2 mixture (15/85) is utilized to simulate the major components of flue gas. As shown in Fig. 6A, no apparent capacity loss is observed after 21 cycles with a mass change of 4.5%, indicating that MIL-53(Al)–NH_2 (200) is capable of withstanding cyclic exposure to the gas mixture and able to remove CO_2 from flue gases.

Beyond application in gas separation, MIL-53(Al)–NH_2 hollow fibers produced under several conditions were further investigated for their catalytic activity for VOC formaldehyde (HCHO) oxidation.[69–71] Results were compared to those of the MIL-53(Al)–NH_2 powder. HCHO removal performance was measured statically in an airtight reactor, with samples cyclically and automatically taken at 1 minute intervals and monitored by utilizing a photoacoustic IR multigas monitor for appearance of CO_2 and decrease of HCHO.[72] The data clearly indicate a heterogeneous removal of HCHO [69–71] on each MIL-53(Al)–NH_2 sample. The adsorption–degradation–desorption process active in this system produces the expected HCHO reduction and CO_2 generation (Fig. 6B and C).[70] The catalytic activity performance is determined by the variation of HCHO concentration after 60 min (Fig. 6B). Results confirm that MIL-53(Al)–NH_2 (200) with the hollow structure shows the best HCHO catalytic activity, followed by MIL-53(Al)–NH_2 (CDA), MIL-53(Al)–NH_2 (powder) and MIL-53(Al)–NH_2 (PP). The superior performance of MIL-53(Al)–NH_2 (200) is ascribed to the unique hollow fiber structure. In part, the radial growth of MOF crystals along with fiber cylinders can diminish most aggregation effects seen in the powder phase. The hollow structure facilitates HCHO molecule flow into the inner side of the cylinders, thereby encountering more active sites. It is worth noting that MIL-53(Al)–NH_2 (200) exhibits excellent reproducibility in HCHO removal analysis, even with a tiny dosage (*ca.* 35

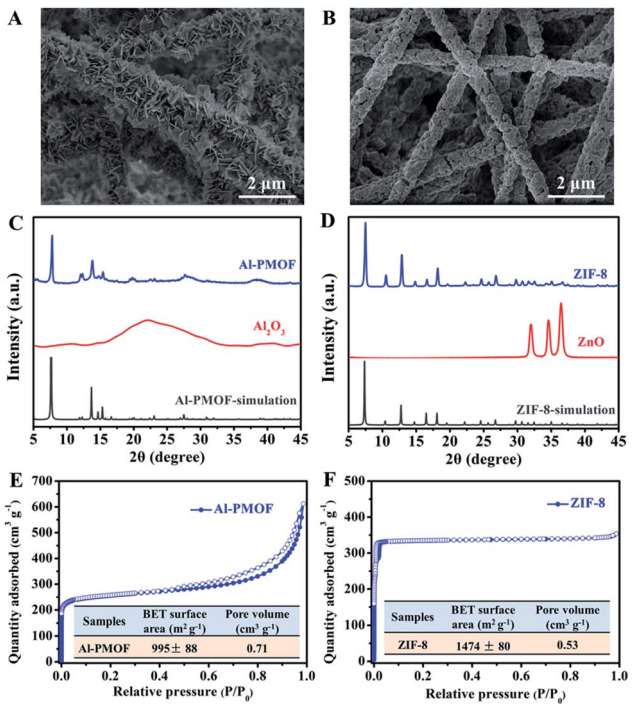

Fig. 4 SEM images of the (A) Al-PMOF predominant fiber mat and (B) ZIF-8 predominant fiber mat. Freestanding fiber structures are retained from their parent phases of Al_2O_3 and ZnO nanofibers, respectively. XRD patterns of (C) Al-PMOF and (D) ZIF-8, which confirm that both Al-PMOF and ZIF-8 have been converted successfully and the characteristic peaks are identical to the simulation patterns. N_2 isotherms of (E) Al-PMOF and (F) ZIF-8 at 77 K. Inset shows the decent BET surface areas and pore volumes of Al-PMOF and ZIF-8.

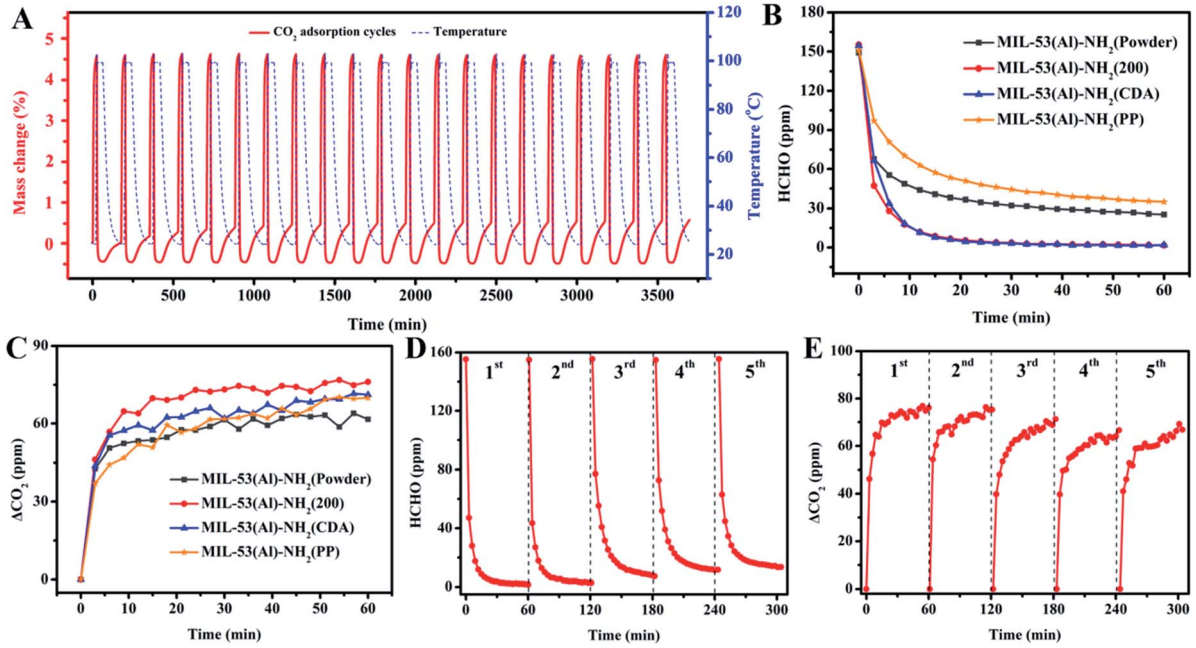

Fig. 6 (A) Cyclic CO_2 adsorption behavior measured by the thermogravimetric method with introducing a 15% CO_2 mixture in N_2 at 25 °C. The initial mass was normalized to 0% at 25 °C under a N_2 atmosphere. HCHO removal tests over MIL-53(Al)–NH_2 (powder), MIL-53(Al)–NH_2 (200), MIL-53(Al)–NH_2 (CDA) and MIL-53(Al)–NH_2 (PP): variation of the concentration of (B) HCHO; (C) CO_2. Reproducibility tests of HCHO removal performance on MIL-53(Al)–NH_2 (200): variation of the concentration of (D) HCHO; (E) CO_2. (F) Proposed heterogeneous catalytic mechanism in HCHO removal using MIL-53(Al)–NH_2 (200) as a catalyst.

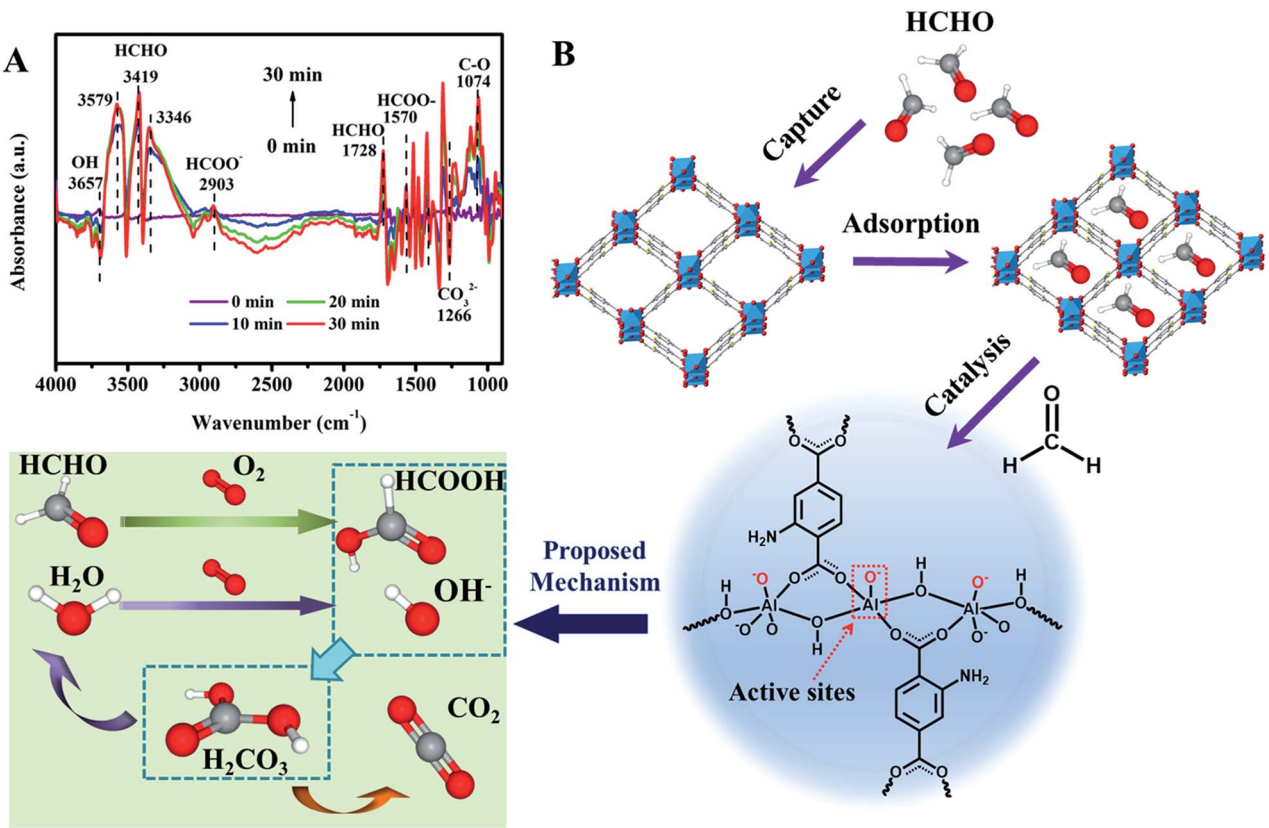

Fig. 7 (A) *In situ* DRIFTS spectra of MIL-53(Al)–NH_2 (200) exposed to a flow of ~80 ppm of HCHO/synergetic air at room temperature. (B) Proposed heterogeneous catalytic mechanism in HCHO removal using MIL-53(Al)–NH_2 (200) as a catalyst.

mg), and still retains the HCHO removal ability of around 92.9% after 5 cyclic tests (Fig. 6D and E). Moreover, the morphology of the MIL-53(Al)–NH_2 (200) fiber mats remains intact after HCHO removal testing (Fig. S12†), indicating good stability of the MOF structure. The VOC removal performance of selected MOFs is summarized in Table S3.† In comparison with other MOFs, MIL-53(Al)–NH_2 (200) shows competitive performance in overall VOC removal.

To demonstrate the degradation pathway of HCHO on MIL-53(Al)–NH_2 (200), *in situ* observation of DRIFTS spectra exposed to a flow of ~80 ppm HCHO/synthetic air within 30 min was recorded at room temperature. As shown in Fig. 7A, characteristic peaks around 1728 cm^{-1}, 3346 cm^{-1}, 3419 cm^{-1}, and 3579 cm^{-1} can be ascribed to gas HCHO (National Institute of Standards and Technology (NIST) Standard Reference Database 69), indicating quick adsorption by the porous MOF structure. The formation of formate species (1570 cm^{-1}, 2903 cm^{-1}) and carbonate species (1266 cm^{-1}) can be clearly observed in the spectra, revealing that the formate species are the main intermediates during the HCHO oxidation process.[73,74] The negative signals around 3657 cm^{-1} can be assigned to surface hydroxyl groups. Based on the results, the proposed mechanism of HCHO removal on MIL-53(Al)–NH_2 (200) is illustrated in Fig. 7B. The heterogeneous catalytic process is composed of several intermediate details. In detail, HCHO molecules are adsorbed by the porous structures initially and then oxidized by $AlO_4(OH)_2$ clusters to transform to formate and carbonate species, finally degrading to harmless products of CO_2 and H_2O.

Conclusions

This work demonstrates a novel approach to fabricate freestanding MIL-53(Al)–NH_2 fiber mats in a unique hollow structure with high crystallinity and porosity. The method can also be extended to other MOF systems with a freestanding hollow structure. The freestanding MOF-fiber mat converted from the metal oxide source formed by ALD shows a well-controlled crystal size and more stable pore configuration as well as a restrained breathing behavior in a flexible MOF structure compared with its powder phase. Experimental analysis confirms that predominant MIL-53(Al)–NH_2 hollow fiber mats have promising potential in CO_2 adsorption, CO_2/N_2 separation, and VOC abatement applications.

Conflicts of interest

There are no conflicts to declare.

Acknowledgements

Part of this work was performed at the Analytical Instrumentation Facility (AIF) at North Carolina State University, which is supported by the State of North Carolina and the National Science Foundation (award number ECCS-1542015). The AIF is a member of the North Carolina Research Triangle Nanotechnology Network (RTNN), a site in the National Nanotechnology Coordinated Infrastructure (NNCI). GNP acknowledges support from the U.S. National Science Foundation, Award No. 1704151. Z. D. acknowledges the China Scholarship Council (CSC) from the Ministry of Education of P. R. China for two-year financial support of studying at North Carolina State University (File No. 201706630121). Z. D. acknowledges support from the Fundamental Research Funds for the Central Universities (No. CUSF-DH-D-2017010). We thank Professor Saad Khan for providing access to the electrospinning setup. We thank Seung Keun Song and Jungsik Kim for XPS measurements and Jiafei Su from Shanghai Normal University for the measurement of HCHO catalytic activity tests.

Notes and references

1 H. Li, M. Eddaoudi, M. O'Keeffe and O. M. Yaghi, *Nature*, 1999, **402**, 276–279.
2 L. F. Chen and Q. Xu, *Science*, 2017, **358**, 304–305.
3 T. Rodenas, I. Luz, G. Prieto, B. Seoane, H. Miro, A. Corma, F. Kapteijn, F. Xamena and J. Gascon, *Nat. Mater.*, 2015, **14**, 48–55.
4 H. Furukawa, K. E. Cordova, M. O'Keeffe and O. M. Yaghi, *Science*, 2013, **341**, 1230444.
5 X. D. Zhang, Y. Yang, L. Song, J. F. Chen, Y. Q. Yang and Y. X. Wang, *J. Hazard. Mater.*, 2019, **365**, 597–605.
6 X. D. Zhang, Y. Yang, X. T. Lv, Y. X. Wang, N. Liu, D. Chen and L. F. Cui, *J. Hazard. Mater.*, 2019, **366**, 140–150.
7 X. D. Zhang, X. T. Lv, X. Y. Shi, Y. Yang and Y. Q. Yang, *J. Colloid Interface Sci.*, 2019, **539**, 152–160.
8 X. D. Zhang, Y. Yang, W. Y. Huang, Y. Q. Yang, Y. X. Wang, C. He, N. Liu, M. H. Wu and L. Tang, *Mater. Res. Bull.*, 2018, **99**, 349–358.
9 N. Liu, W. Y. Huang, M. Q. Tang, C. C. Yin, B. Gao, Z. M. Li, L. Tang, J. Q. Lei, L. F. Cui and X. D. Zhang, *Chem. Eng. J.*, 2019, **359**, 254–264.
10 X. Zhang, X. Lv, F. Bi, G. Lu and Y. Wang, *Mol. Catal.*, 2019, 110701, DOI: 10.1016/j.mcat.2019.110701.
11 X. D. Zhang, X. L. Zhang, L. Song, F. L. Hou, Y. Q. Yang, Y. X. Wang and N. Liu, *Int. J. Hydrogen Energy*, 2018, **43**, 18279–18288.
12 Y. Q. Yang, H. Dong, Y. Wang, C. He, Y. X. Wang and X. D. Zhang, *J. Solid State Chem.*, 2018, **258**, 582–587.
13 X. D. Zhang, Y. Yang, L. Song, Y. X. Wang, C. He, Z. Wang and L. F. Cui, *Mol. Catal.*, 2018, **447**, 80–89.
14 X. D. Zhang, F. L. Hou, Y. Yang, Y. X. Wang, N. Liu, D. Chen and Y. Q. Yang, *Appl. Surf. Sci.*, 2017, **423**, 771–779.
15 Y. Wang, Y. Q. Yang, N. Liu, Y. X. Wang and X. D. Zhang, *RSC Adv.*, 2018, **8**, 33096–33102.
16 X. J. Ma, Y. T. Chai, P. Li and B. Wang, *Acc. Chem. Res.*, 2019, **52**, 1461–1470.
17 Y. F. Chen, S. H. Zhang, S. J. Cao, S. Q. Li, F. Chen, S. Yuan, C. Xu, J. W. Zhou, X. Feng, X. J. Ma and B. Wang, *Adv. Mater.*, 2017, **29**, 1606221.
18 J. J. Zhao, D. T. Lee, R. W. Yaga, M. G. Hall, H. F. Barton, I. R. Woodward, C. J. Oldham, H. J. Walls, G. W. Peterson and G. N. Parsons, *Angew. Chem., Int. Ed.*, 2016, **55**, 13224–13228.

19 D. T. Lee, J. J. Zhao, G. W. Peterson and G. N. Parsons, *Chem. Mater.*, 2017, **29**, 4894–4903.
20 X. L. Ma, P. Kumar, N. Mittal, A. Khlyustova, P. Daoutidis, K. A. Mkhoyan and M. Tsapatsis, *Science*, 2018, **361**, 1008–1011.
21 S. L. Qiu, M. Xue and G. S. Zhu, *Chem. Soc. Rev.*, 2014, **43**, 6116–6140.
22 D. T. Lee, J. D. Jamir, G. W. Peterson and G. N. Parsons, *Small*, 2019, **15**, 1805133.
23 Y. Y. Zhang, S. Yuan, X. Feng, H. W. Li, J. W. Zhou and B. Wang, *J. Am. Chem. Soc.*, 2016, **138**, 5785–5788.
24 Y. C. Lin, C. L. Kong, Q. J. Zhang and L. Chen, *Adv. Energy Mater.*, 2017, **7**, 1601296.
25 A. Pustovarenko, M. G. Goesten, S. Sachdeva, M. X. Shan, Z. Amghouz, Y. Belmabkhout, A. Dikhtiarenko, T. Rodenas, D. Keskin, I. K. Voets, B. M. Weckhuysen, M. Eddaoudi, L. de Smet, E. J. R. Sudholter, F. Kapteijn, B. Seoane and J. Gascon, *Adv. Mater.*, 2018, **30**, 1707234.
26 H. X. Liang, X. L. Jiao, C. Li and D. R. Chen, *J. Mater. Chem. A*, 2018, **6**, 334–341.
27 P. Horcajada, R. Gref, T. Baati, P. K. Allan, G. Maurin, P. Couvreur, G. Ferey, R. E. Morris and C. Serre, *Chem. Rev.*, 2012, **112**, 1232–1268.
28 H. X. Liang, A. N. Yao, X. L. Jiao, C. Li and D. R. Chen, *ACS Appl. Mater. Interfaces*, 2018, **10**, 20396–20403.
29 D. B. Dwyer, D. T. Lee, S. Boyer, W. E. Bernier, G. N. Parsons and W. E. Jones, *ACS Appl. Mater. Interfaces*, 2018, **10**, 25794–25803.
30 J. Reboul, S. Furukawa, N. Horike, M. Tsotsalas, K. Hirai, H. Uehara, M. Kondo, N. Louvain, O. Sakata and S. Kitagawa, *Nat. Mater.*, 2012, **11**, 717–723.
31 K. Khaletskaya, S. Turner, M. Tu, S. Wannapaiboon, A. Schneemann, R. Meyer, A. Ludwig, G. Van Tendeloo and R. A. Fischer, *Adv. Funct. Mater.*, 2014, **24**, 4804–4811.
32 J. J. Zhao, M. D. Losego, P. C. Lemaire, P. S. Williams, B. Gong, S. E. Atanasov, T. M. Blevins, C. J. Oldham, H. J. Walls, S. D. Shepherd, M. A. Browe, G. W. Peterson and G. N. Parsons, *Adv. Mater. Interfaces*, 2014, **1**, 1400040.
33 Z. J. Dai, X. W. Yu, C. Huang, M. Li, J. F. Su, Y. P. Guo, H. Xu and Q. F. Ke, *RSC Adv.*, 2016, **6**, 97022–97029.
34 A. Boutin, S. Couck, F. X. Coudert, P. Serra-Crespo, J. Gascon, F. Kapteijn, A. H. Fuchs and J. F. M. Denayer, *Microporous Mesoporous Mater.*, 2011, **140**, 108–113.
35 S. Couck, E. Gobechiya, C. E. A. Kirschhock, P. Serra-Crespo, J. Juan-Alcaniz, A. M. Joaristi, E. Stavitski, J. Gascon, F. Kapteijn, G. V. Baron and J. F. M. Denayer, *ChemSusChem*, 2012, **5**, 740–750.
36 N. Alvarez-Gutierrez, M. V. Gil, F. Rubiera and C. Pevida, *Fuel Process. Technol.*, 2016, **142**, 361–369.
37 A. Corma, V. Fornes, S. B. Pergher, T. L. M. Maesen and J. G. Buglass, *Nature*, 1998, **396**, 353–356.
38 M. Choi, K. Na, J. Kim, Y. Sakamoto, O. Terasaki and R. Ryoo, *Nature*, 2009, **461**, 246–249.
39 X. D. Zhang, H. X. Li, X. T. Lv, J. C. Xu, Y. X. Wang, C. He, N. Liu, Y. Q. Yang and Y. Wang, *Chem.–Eur. J.*, 2018, **24**, 8822–8832.
40 X. D. Zhang, H. X. Li, F. L. Hou, Y. Yang, H. Dong, N. Liu, Y. X. Wang and L. F. Cui, *Appl. Surf. Sci.*, 2017, **411**, 27–33.
41 X. D. Zhang, F. L. Hou, H. X. Li, Y. Yang, Y. X. Wang, N. Liu and Y. Q. Yang, *Microporous Mesoporous Mater.*, 2018, **259**, 211–219.
42 P. Serra-Crespo, E. Gobechiya, E. V. Ramos-Fernandez, J. Juan-Alcaniz, A. Martinez-Joaristi, E. Stavitski, C. E. A. Kirschhock, J. A. Martens, F. Kapteijn and J. Gascon, *Langmuir*, 2012, **28**, 12916–12922.
43 H. R. Abid, Z. H. Rada, X. Duan, H. Sun and S. Wang, *Energy Fuels*, 2018, **32**, 4502–4510.
44 M. Bechelany, M. Drobek, C. Vallicari, A. Abou Chaaya, A. Julbe and P. Miele, *Nanoscale*, 2015, **7**, 5794–5802.
45 C. M. Moran, J. N. Joshi, R. M. Marti, S. E. Hayes and K. S. Walton, *J. Am. Chem. Soc.*, 2018, **140**, 9148–9153.
46 H. Robatjazi, D. Weinberg, D. F. Swearer, C. Jacobson, M. Zhang, S. Tian, L. N. Zhou, P. Nordlander and N. J. Halas, *Sci. Adv.*, 2019, **5**, eaav5340.
47 K. Okada, R. Ricco, Y. Tokudome, M. J. Styles, A. J. Hill, M. Takahashi and P. Falcaro, *Adv. Funct. Mater.*, 2014, **24**, 1969–1977.
48 J. Cravillon, R. Nayuk, S. Springer, A. Feldhoff, K. Huber and M. Wiebcke, *Chem. Mater.*, 2011, **23**, 2130–2141.
49 E. J. Carrington, C. A. McAnally, A. J. Fletcher, S. P. Thompson, M. Warren and L. Brammer, *Nat. Chem.*, 2017, **9**, 882–889.
50 S. B. Choi, H. Furukawa, H. J. Nam, D.-Y. Jung, Y. H. Jhon, A. Walton, D. Book, M. O'Keeffe, O. M. Yaghi and J. Kim, *Angew. Chem., Int. Ed.*, 2012, **51**, 8791–8795.
51 L. Bolinois, T. Kundu, X. R. Wang, Y. X. Wang, Z. G. Hu, K. Koh and D. Zhao, *Chem. Commun.*, 2017, **53**, 8118–8121.
52 Y. Sakata, S. Furukawa, M. Kondo, K. Hirai, N. Horike, Y. Takashima, H. Uehara, N. Louvain, M. Meilikhov, T. Tsuruoka, S. Isoda, W. Kosaka, O. Sakata and S. Kitagawa, *Science*, 2013, **339**, 193–196.
53 W. P. Mounfield and K. S. Walton, *J. Colloid Interface Sci.*, 2015, **447**, 33–39.
54 A. Boutin, F. X. Coudert, M. A. Springuel-Huet, A. V. Neimark, G. Ferey and A. H. Fuchs, *J. Phys. Chem. C*, 2010, **114**, 22237–22244.
55 T. Ahnfeldt, D. Gunzelmann, T. Loiseau, D. Hirsemann, J. Senker, G. Ferey and N. Stock, *Inorg. Chem.*, 2009, **48**, 3057–3064.
56 T. Lescouet, E. Kockrick, G. Bergeret, M. Pera-Titus, S. Aguado and D. Farrusseng, *J. Mater. Chem.*, 2012, **22**, 10287–10293.
57 F. Zhang, X. Q. Zou, X. Gao, S. J. Fan, F. X. Sun, H. Ren and G. S. Zhu, *Adv. Funct. Mater.*, 2012, **22**, 3583–3590.
58 K. Sumida, D. L. Rogow, J. A. Mason, T. M. McDonald, E. D. Bloch, Z. R. Herm, T. H. Bae and J. R. Long, *Chem. Rev.*, 2012, **112**, 724–781.
59 A. O. Yazaydin, R. Q. Snurr, T. H. Park, K. Koh, J. Liu, M. D. LeVan, A. I. Benin, P. Jakubczak, M. Lanuza, D. B. Galloway, J. J. Low and R. R. Willis, *J. Am. Chem. Soc.*, 2009, **131**, 18198.
60 J. M. Yu, L. H. Xie, J. R. Li, Y. G. Ma, J. M. Seminario and P. B. Balbuena, *Chem. Rev.*, 2017, **117**, 9674–9754.

61 J. R. Li, J. M. Yu, W. G. Lu, L. B. Sun, J. Sculley, P. B. Balbuena and H. C. Zhou, *Nat. Commun.*, 2013, **4**, 1538.
62 M. Wriedt, J. P. Sculley, A. A. Yakovenko, Y. G. Ma, G. J. Halder, P. B. Balbuena and H. C. Zhou, *Angew. Chem., Int. Ed.*, 2012, **51**, 9804–9808.
63 A. L. Myers and J. M. Prausnitz, *AIChE J.*, 1965, **11**, 121.
64 J. A. Mason, K. Sumida, Z. R. Herm, R. Krishna and J. R. Long, *Energy Environ. Sci.*, 2011, **4**, 3030–3040.
65 T. M. McDonald, D. M. D'Alessandro, R. Krishna and J. R. Long, *Chem. Sci.*, 2011, **2**, 2022–2028.
66 R. Sips, *J. Chem. Phys.*, 1948, **16**, 490–495.
67 D. D. Do, *Adsorption Analysis: Equilibria and Kinetics*, 1998, DOI: 10.1142/p111.
68 K. H. Shi, E. E. Santiso and K. E. Gubbins, *Langmuir*, 2019, **35**, 5975–5986.
69 J. L. Wang, J. Li, P. Y. Zhang and G. K. Zhang, *Appl. Catal., B*, 2018, **224**, 863–870.
70 S. Rong, P. Zhang, F. Liu and Y. Yang, *ACS Catal.*, 2018, **8**, 3435–3446.
71 J. Q. Torres, S. Royer, J. P. Bellat, J. M. Giraudon and J. F. Lamonier, *ChemSusChem*, 2013, **6**, 578–592.
72 Z. J. Dai, J. F. Su, X. M. Zhu, K. L. Xu, J. Zhu, C. Huang and Q. F. Ke, *J. Mater. Chem. A*, 2018, **6**, 14856–14866.
73 L. Zhu, J. L. Wang, S. P. Rong, H. Y. Wang and P. Y. Zhang, *Appl. Catal., B*, 2017, **211**, 212–221.
74 F. Liu, S. P. Rong, P. Y. Zhang and L. L. Gao, *Appl. Catal., B*, 2018, **235**, 158–167.

Supporting Information

Fabrication of Freestanding Metal Organic Framework Predominant Hollow Fiber Mat and Its Potential Applications in Gas Separation and Catalysis

Zijian Dai [a,b], *Dennis T. Lee* [b], *Kaihang Shi* [b], *Siyao Wang* [b], *Heather F. Barton* [b], *Jie Zhu* [c], *Jiaqi Yan* [b], *Qinfei Ke* [a,*], *and Gregory N. Parsons* [b,*]

a Key Laboratory of Textile Science & Technology, Ministry of Education, College of Textiles, Donghua University, Shanghai, 201620, China

b Department of Chemical & Biomolecular Engineering, North Carolina State University, 911 Partners Way, Raleigh, North Carolina 27695, United States

c School of Fashion Engineering, Shanghai University of Engineering Science, No.333 Longteng Road, Songjiang, Shanghai, 201620, China

Section 1-Materials and Synthesis

1. Materials

Cellulose diacetate (CDA, Eastman Chemicals), diethyl zinc (DEZ, 95% STREM Chemicals Inc.,), trimethyl aluminum (TMA, 98% STREM Chemicals Inc.,), 2-amino-terephthalic acid (99%, Acros Organics), aluminum chloride hexahydrate ($AlCl_3 \cdot 6H_2O$, Alfa Aesar), copper nitrate trihydrate ($Cu(NO_3)_2 \cdot 3H_2O$, 99-104%, Sigma-Aldrich), 2-methylimidazole (99%, Sigma-Aldrich), meso-Tetra (4-carboxyphenyl) porphine (H_2TCPP, >97% Frontier Scientific), acetone (Fisher), N,N-dimethylformamide (DMF, Fisher), N,N-dimethylacetamide (DMAc, 99.8%, Sigma-Aldrich), anhydrous ethanol (200 proof, VWR), were purchased from commercial sources and used without further treatment. Melt-blown polypropylene (PP) fiber mats with density of 40 gsm was used as received from Nonwovens Cooperative Research Center (NCRC), North Carolina State University.

2. Fabrication of Cellulose Diacetate Nanofiber Mats

CDA nanofiber mats were fabricated by electrospinning technique. The electrospinning system used in this experiment consisted of a high voltage power supply (Precision Inc.,), a syringe pump (New Era Pump System Inc.,) and a conductive collector. Briefly, CDA was dissolved overnight in acetone/DMAc (2:1, v/v) to reach a CDA final concentration of 11 wt%. The polymer solution was then loaded into a plastic syringe with a 27 gauge stainless needle. The feed rate of 0.5 mL h^{-1} and a 13 kV voltage were controlled. The collection distance was fixed at 15 cm and the as-spun CDA nanofiber mats were collected on the metallic collector covered with aluminum foil. Electrospinning was performed at ambient temperature and the relative humidity was maintained at around 60%.

3. Atomic Layer Deposition of Al_2O_3 and ZnO on CDA Nanofiber Mats

CDA nanofiber mats were conformally coated with Al_2O_3 and ZnO thin films using a homebuilt hot-wall viscous-flow ALD reactor as previous work described[1]. ALD deposition with the metal oxide of Al_2O_3 and ZnO was both conducted at 90 ^oC under ~1.8 Torr. In a typical ALD Al_2O_3 cycle, TMA was first dosed to the reactor chamber for 2 s, followed by N_2 purge for 40 s. After another 2 s of H_2O dosing, the chamber was swept by N_2 for 60 s to complete one ALD running cycle. While in ALD ZnO process, the dose time of the DEZ precursors was set to 2s with a different interval of N_2 purge of 60 s. These as-prepared samples were referred as CDA@Al_2O_3 and CDA@ZnO, respectively.

4. Synthesis of MIL-53(Al)-NH_2 Powder

MIL-53(Al)-NH_2 powders were synthesized adapting from previous reports[2]. $AlCl_3 \cdot 6H_2O$ (0.966 g) was picked up as metal source, mixed with 2-amino-terephthalic acid (0.725 g) dissolved in 20 mL co-solvent mix solution (DMF/Water = 3/1, v/v) which is derived after the pre-experiments. The mixture was then transferred into a 100 mL Telfon-lined stainless-steel autoclave reactor and heated at 150 ^oC for 24 h. After cooling, the MIL-53(Al)-NH_2 product was washed twice by hot DMF for 24 h to remove unreacted 2-amino-terephthalic acid linkers and collected by filtration. After that, the powders were washed by anhydrous ethanol for another two times to remove DMF. The resulting materials were finally dried and burned under vacuum at 200 ^oC for 10 h.

5. Synthesis of MIL-53(Al)-NH_2 Predominant Hollow Fiber Mats

To synthesize MIL-53(Al)-NH_2 predominant hollow fiber mats, the CDA@Al_2O_3 nanofiber mat was first immersed in acetone and heated up to 120 ^oC for 24 h to dissolve and remove

out the CDA polymers. After the delicate treatment, the majority of CDA polymers (~ 90%) were removed out from the CDA@Al_2O_3 nanofiber mats, left with an Al_2O_3 hollow fiber mats with tiny polymer residuals. For the conversion of MIL-53(Al)-NH_2 using Al_2O_3 hollow fiber mats as the metal source, 0.106 g 2-amino-terephthalic acid was firstly added to a 20 mL DMF/ water mixture (3/1, v/v), then the mixture was sonicated and stirred for 20 min until complete dissolution. Subsequently, a piece of Al_2O_3 hollow fiber mat (0.030 g) was gently soaked in the prepared solution and transferred into a 100 mL Telfon-lined stainless-steel autoclave reactor. This reactor was then heated at 120 ^oC for 20 h to finish the solvothermal synthesis. After complete reaction, the as-received MIL-53(Al)-NH_2 hollow fiber mat was washed twice with hot DMF, followed by another 2 times of anhydrous ethanol washing. The MIL-53(Al)-NH_2 hollow fiber mat was finally dried under vacuum at 200 ^oC for 10 h and stored in a desiccator before test. As a control group, CDA@Al_2O_3 nanofiber mat was also converted into MIL-53(Al)-NH_2 directly using the same recipe mentioned above without the pretreatment in acetone solution. The as-prepared sample was denoted as MIL-53(Al)-NH_2 (CDA).

6. Synthesis of MIL-53(Al)-NH_2 onto PP Nonwovens

0.062 g 2-amino-terephthalic acid was dispersed in 20 mL DMF/ water mixtures (3/1, v/v) in 100 mL Telfon-lined stainless-steel autoclave reactor. Subsequently, melt-blown PP fiber mats (1" × 2") coated with 200 cycles of ALD Al_2O_3 (PP@Al_2O_3) were added into the solution. The autoclave was transferred into an oven and heated to 120 ^oC for 20 h. After the reaction done, the MIL-53(Al)-NH_2 (PP) swatch was washed twice with hot DMF and rinsed

with anhydrous ethanol 2 times. The resulting MIL-53(Al)-NH_2 (PP) swatch was dried under vacuum at 120 ^oC for 12 h and stored in a desiccator before other measurements.

7. Synthesis of ZIF-8 Predominant Hollow Fiber Mats

To synthesize ZIF-8 predominant hollow fiber mat, 0.10 g 2-methylimidazole was dispersed into 20 mL DMF. ZnO hollow fiber mat (obtained from dissolving CDA@ZnO into acetone, 0.03g) was subsequently soaked in the solution. The as-prepared precursor mixture was then transferred into a 100 mL Telfon-lined stainless-steel autoclave reactor and heated to 100 ^oC for 10 h. After the reaction done, the as-received ZIF-8 hollow fiber mat was washed twice with hot DMF, followed by another 2 times of anhydrous ethanol washing. The ZIF-8 hollow fiber mat was finally dried under vacuum at 100 ^oC for 10 h and stored in a desiccator before test.

8. Synthesis of Al-TCPP predominant hollow fiber mats

0.23 g H_2TCPP was dissolved in a DMF (5mL) and water mixture (15mL). Subsequently, Al_2O_3 hollow fiber mat (0.03 g) was fully immersed in the solution mixture. The as-prepared precursor mixture was then transferred into a 100 mL Telfon-lined stainless-steel autoclave reactor and heated to 120 ^oC for 20 h. After the reaction done, the as-received Al-TCPP hollow fiber mat was washed twice with hot DMF, followed by another 2 times of anhydrous ethanol washing. The Al-TCPP hollow fiber mat was finally dried under vacuum at 100 ^oC for 10 h and stored in a desiccator before test.

Section 2-Characterization

1. Scanning electron microscopic (SEM) and X-ray photoelectron spectroscopy (XPS)

SEM was conducted using a FEI Verios 460 L field emission SEM. X-ray diffraction (XRD) was taken with a Rigaku SmartLab X-ray diffraction tool (Cu Kα X-ray source) for crystalline structure characterization. XPS was performed on a Kratos Analytical Axis Ultra system equipped with aluminum gun (Al Kα = 1486.6 eV radiation). Voltage and current of x-ray gun was 15 kV and 20 mA. All the binding energies were calibrated using contaminated carbon (C1s = 284.6 eV).

2. Thermogravimetric Analysis and CO_2 Cycling Measurement

CO_2 cycling experiments were carried out on a TA instruments SDT 650. 15% CO_2/N_2 (Acro) and N_2 (99.999%) were used in this experiment. In a typical test, ~10 mg target sample was loaded into an alumina pan, with a flow rate of 100 mL/min for both gases. The sample was first heated at 100 ^oC for 40 min under N_2 atmosphere to complete degassing, after the temperature was cooling down to 25 ^oC, MOF sample was swept continuously by CO_2 for 20 min, and then flowing N_2 was maintained for 40 min at 100 ^oC for activating MOF sample in every cycle.

3. Adsorption and Catalytic Activity Test

The HCHO adsorption and catalytic activities were evaluated in static state which was adapted from previous reports[3]. A polytetrafluoroethylene layer stainless steel reactor (0.5 L) was used, at the bottom of which was placed a quartz Petri dish with swatch inside. After putting the dish into the reactor, 300 ppm of HCHO which was generated from S-4000 Gas Mixing system (Environics, USA) was injected into the reactor. After stabilizing the concentration of HCHO to 150 ppm, the cover of the dish was removed to start the adsorption and catalytic reaction of HCHO. HCHO, CO_2, CO and water vapor were recorded online by a

photoacoustic IR multigas monitor (INNOVA AirTech Instruments Model 1412i) during test at 25 ^{o}C. The yield of CO_2 (ΔCO_2) and the concentration variation of HCHO were calculated to analyze the HCHO removal ratio.

Section 3-Calculation of MOF Conversion Ratio

General

The conversion ratio of MOFs based on ALD precursors was calculated by adapting equations first published by Bechelany's group.

Equation

x = quantity (mol) of metal in the oxide

y = quantity (mol) of metal in the MOF

A = total quantity (mol) of metal in the MOF hollow fiber mats

B = final weight of the MOF hollow fiber mats

M_Wx = oxide molecular weight (g/mol)

M_Wy = MOF molecular weight (g/mol)

As far as the metal loss was not detected during the synthesis, A was considered as a constant:

$$A = x + y \tag{S1}$$

The final weight of the MOF hollow fiber mats is written as (Al_2O_3 is chosen as metal source):

$$B = \frac{X}{2} \times M_W x + y \times M_W y \tag{S2}$$

By replacing (x = A-y) in (S2), y can be calculated by:

$$y = (2B - A \times M_W x) \div (2M_W y - M_W x) \tag{S3}$$

The conversion ratio can thus be written as follows:

$$Conversion\ ratio = 100 \times (y \div A) = 100 \times [(2B - A \times M_W x) \div (2M_W y - M_W x)] \div A \quad \text{(S4)}$$

Section 4-Results

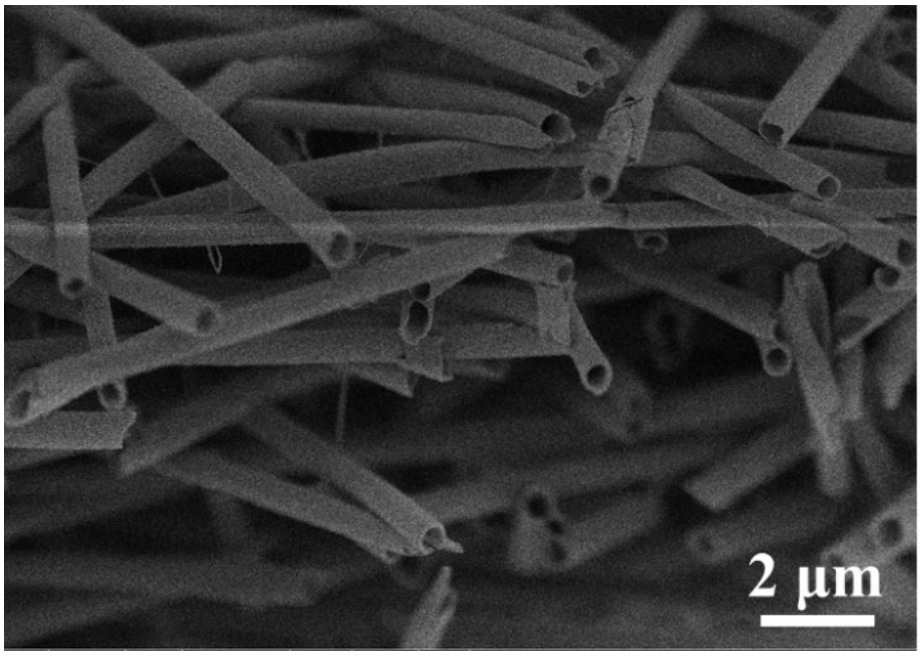

Figure S1. Cross-sectional SEM image of hollow Al_2O_3 fiber mat.

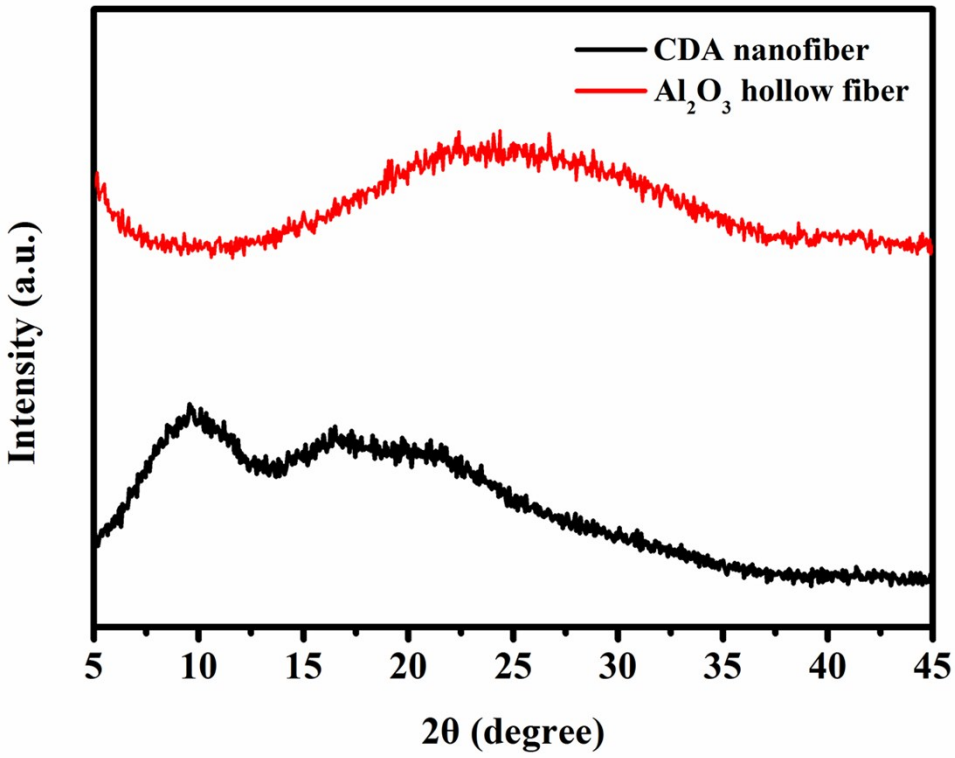

Figure S2. XRD pattern of pristine CDA nanofiber and Al_2O_3 hollow fiber mat obtained from rising Al_2O_3/CDA in acetone at 120 ^oC for 12 h.

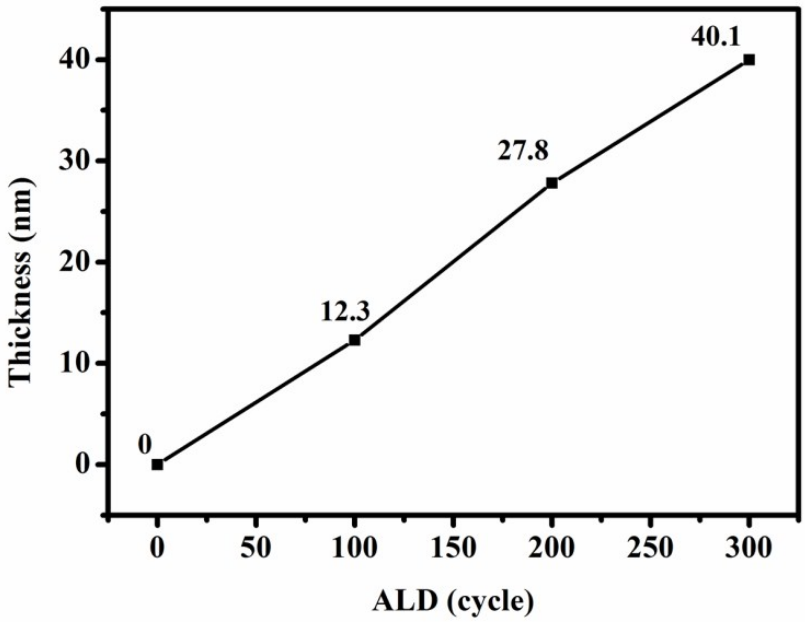

Figure S3. Al_2O_3 real thickness as a function of running cycles.

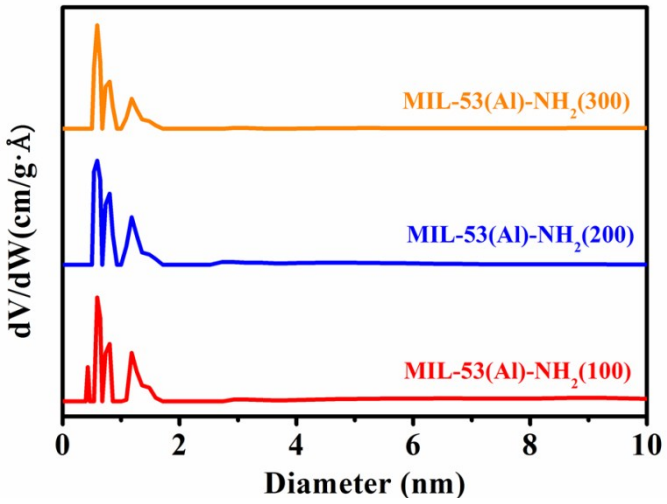

Figure S4. Pore size distribution curves: DFT at 77 K of MIL-53(Al)-NH_2 (100), MIL-53(Al)-NH_2 (200), and MIL-53(Al)-NH_2 (300).

Figure S5. Optical photographs of (a) MIL-53(Al)-NH_2 (100), (b) MIL-53(Al)-NH_2 (200), and (c) MIL-53(Al)-NH_2 (300).

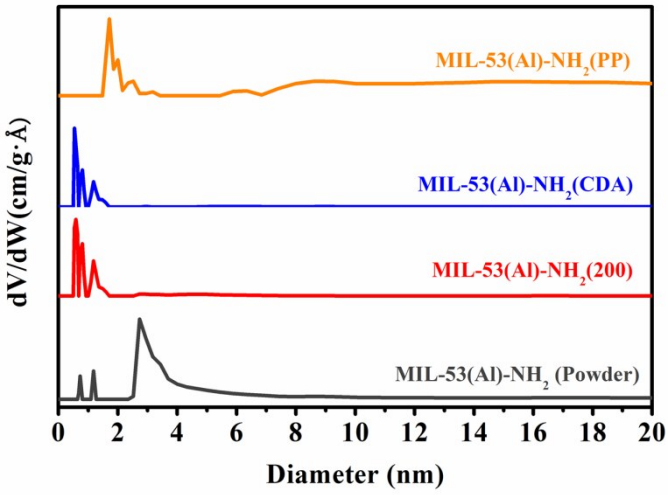

Figure S6. Pore size distribution curves: DFT at 77 K of MIL-53(Al)-NH_2 (powder), MIL-53(Al)-NH_2 (200), MIL-53(Al)-NH_2 (CDA) and MIL-53(Al)-NH_2 (PP).

Table S1. Physical parameters and CO_2 adsorption uptake in selected MIL-53(Al)-NH_2

MOF	Surface areas S_{BET} (m^2 g^{-1})	Pore volume V_p (cm^3 g^{-1})	Conversion ratio (%)	CO_2 adsorption capacity (mmol g^{-1})			$S_{CO2/N2}$ [a]	Ref
				bar	273 K	298K		
MIL-53(Al)-NH_2 (100)	880 ± 30	0.76	100	1	3.91 ± 0.1	1.81	-	This work
MIL-53(Al)-NH_2 (200)	842 ± 28	0.65	97	1	3.30 ± 0.05	1.65		This work
MIL-53(Al)-NH_2 (300)	720 ± 40	0.50	74	1	2.65 ± 0.08	1.45	-	This work
MIL-53(Al)-NH_2 (powder)	1089 ± 112	0.62	-	1	2.35 ± 0.11	2.16		This work
MIL-53(Al)-NH_2 (CDA)	480 ± 21	0.28	-	1	1.98 ± 0.13	1.29		This work
MIL-53(Al)-NH_2 (PP)	3.55 ± 2.7	0.009	-	1	0.17 ± 0.01	0.10		This work
MIL-53-NH_2 (membrane)	-	-	-	1	3.09	2.14	-	[4]
MIL-53-NH_2 (powder)	-	-	-	1	2.24	-	-	[5]
MIL-53 (powder)	905	0.40	-	-	-	-		[6]
MIL-53-NH_2 (powder)	400	1.03	-	1	2.18	1.88	42.3	[7]

a IAST selectivity based on a gas mixture of 0.15 bar N_2 and 0.85 bar CO_2

Section 5- Experimental and Simulated Sorption Studies

1. Low-pressure Gas Adsorption Measurements.

Gas adsorption isotherms in the pressure range of 0-1.1 bar were measured by a volumetric method using a Micromeritics 3Flex Surface Characterization Analyzer. Before analysis, all samples were fully degassed under vacuum at 120 ^{o}C for 20 h. After the degas process is completed, the sample tubes were weighted and then carefully transferred to the analysis port of the gas adsorption instrument. N_2 adsorption-desorption isotherms at 77 K were measured in liquid nitrogen. N_2 and CO_2 adsorption-desorption isotherms at 273 K were measured using an ice water bath and isotherms at 298 K were measured using water baths. All temperatures were monitored before and after the measurement and no temperature change had been detected in all cases.

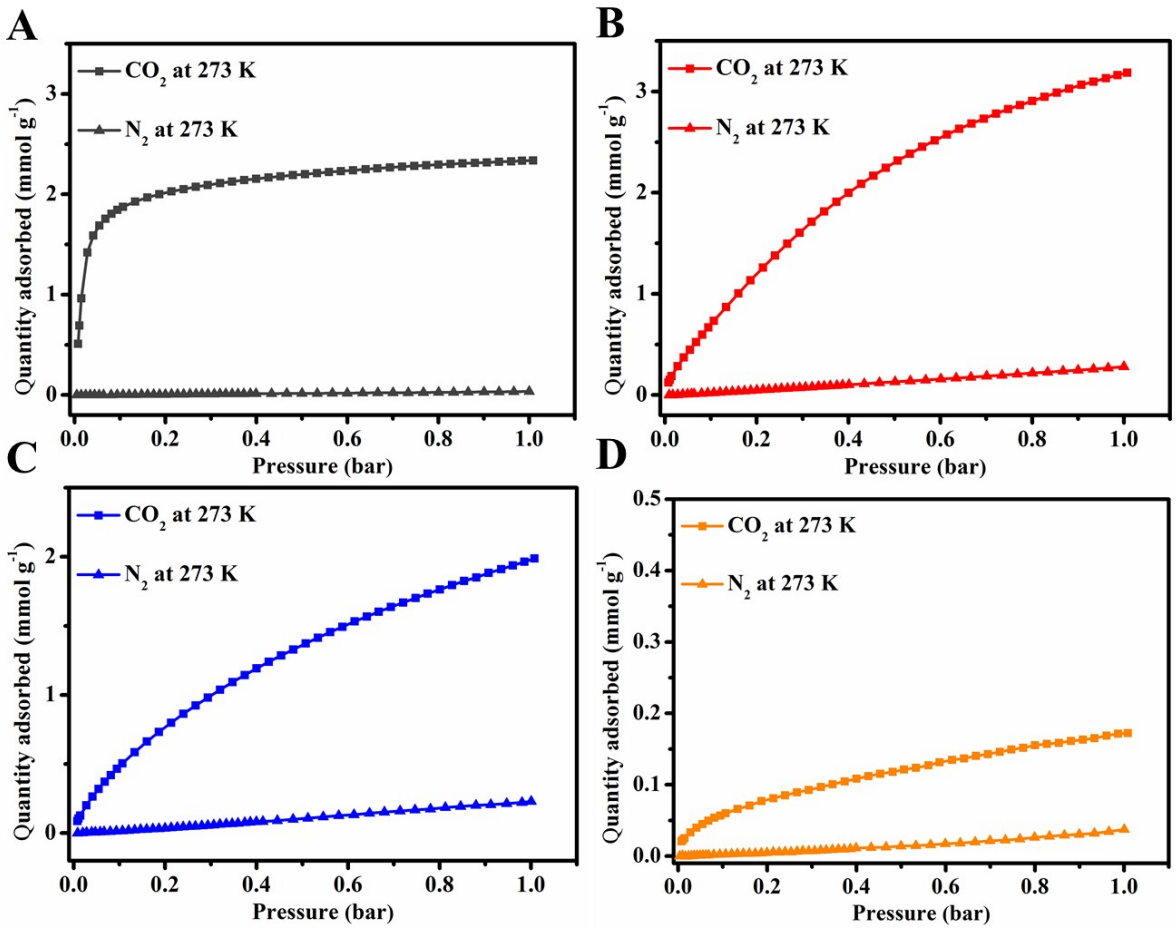

Figure S7. Single component of CO_2 and N_2 adsorption isotherms of (A) MIL-53(Al)-NH_2 (powder), (B) MIL-53(Al)-NH_2 (200), (C) MIL-53(Al)-NH_2 (CDA), and MIL-53(Al)-NH_2 (PP) at 273 K.

3. Isotherms from IAST simulations and CO_2/N_2 selectivity

Calculation details

To predict CO_2/N_2 selectivity, we applied the ideal adsorbed solution theory (IAST)[8]. The IAST can predict a mixed-gas adsorption based on the experimental pure isotherm data and requires no data for the mixture. The IAST relates the adsorbed phase and the gas phase using the general thermodynamic equations by assuming an ideal gas phase (which is an excellent approximation for pressure less than 1 atm) and an ideal solution for the adsorbed phase (i.e., activity coefficient is unity). An expression analogous to the Raoult's law can be obtained,

$$Py_i = P_i^0 x_i \tag{S5}$$

where P is the total pressure in the gas phase; y_i is the mole fraction of component *i* in the gas phase; P_i^0 is the pure vapor pressure for component *i* at the temperature T and the spreading pressure π of the adsorbed mixture; and x_i is the mole fraction of component *i* in the adsorbed mixture. In practice, the total pressure P and the mole fraction of each component y_i in the binary-gas phase are usually given, to determine the unknown variables P_i^0 and x_i, we need to resort to the Gibbs adsorption isotherm to calculate the spreading pressure π,

$$\frac{A\pi}{RT} = \int_0^{P_1^0} \frac{n_1(p)}{p} dp = \int_0^{P_2^0} \frac{n_2(p)}{p} dp \quad \text{(S6)}$$

where A is the surface area of adsorbent and R is the gas constant; $n_i(p)$ is the experimental isotherm data for pure component *i* and is a function of pressure, we use lower case p here to indicate that it's a dummy integral variable. The integration in Eq. (S6) needs to be carried out up to a pressure that is usually higher than the experimental pressure limit (1 bar) accessible to the normal vapor sorption analyzer. Thus, fitting the current experimental isotherm data to an adsorption model is required and the isotherm data at any pressure can then be predicted by the fitted equation. The IAST doesn't specify the fitting model for the pure isotherm, any adsorption model could be potentially used here. In this work, we found the Sips equation [9] fits the experimental pure adsorption isotherm data better than the Toth [11] and Langmuir equations [10], so we applied the Sips equation here,

$$n_i = n_s \frac{(bP)^{1/n}}{1+(bP)^{1/n}} \quad \text{(S7)}$$

where n_s, b and n are the saturation adsorption capacity, adsorption equilibrium constant and the parameter characterizing the system heterogeneity, respectively. The heterogeneity of the system may result from the adsorbent or adsorbate or the combination of both [11]; the larger the value n is, the more heterogeneous the system is. The parameter n is temperature dependent, and its value would decrease with the temperature [11]. When $n=1$, Equation. S7 reduces to the Langmuir equation assuming the adsorption on a homogeneous flat surface. Such behavior of the parameter n with the temperature is consistent with the statistical mechanical analysis of the adsorption on heterogeneous surfaces [12, 13].

Now, we have a well-posed math problem, we have four equations (two of Equation S5 for each component, Equation S6 and remembering $x_1 + x_2 = 1$), and four unknown variables (P_i^0 and x_i for each component in a binary mixture). Once we obtain the mole fraction x_i in the adsorbed phase, we can determine the total adsorbed amount based on the fact that there is no molecular area change upon mixing in the ideal adsorbed solution,

$$\frac{1}{n_t} = \frac{x_1}{n_1^0} + \frac{x_2}{n_2^0} \tag{S8}$$

where n_t is the total adsorbed amount for the mixture; n_1^0 and n_2^0 are the adsorbed amount for the pure component at temperature *T* and gas-phase pressure P_1^0 and P_2^0, respectively, and they can be obtained either from experiments or fitted equations [e.g., Equation S7]. The MATLAB code for the IAST calculations has been validated against the reported data [11] and is available on https://github.com/KaihangShi/IAST. The selectivity coefficient has been defined as[8]

$$S = \frac{x_1/x_2}{y_1/y_2} \tag{S9}$$

The quality of fit to the available experimental pure isotherm data is essential to the accuracy of the IAST calculation, and it has been emphasized a lot in real applications[14]. The possible dependence of fitting parameters on the initial guess and constraint bound of the fitting algorithm, however, is generally overlooked, which is especially important for the less-adsorbed component not showing much curvature in its isotherm data. An example is shown in **Figure S**8 where two equations both fit experimental data very well but showing distinct shape at high pressure region. If possible, the experimental isotherm data at high pressure should be collected to reduce the uncertainty in the fitting process.

Here, we fit our pure adsorption isotherm data for CO_2 and N_2 by choosing different initial guesses of the fitting parameters and setting lower bound of those parameters to 0. For CO_2 adsorption in a specific sample at 273 K, the final Sips equation is generally fixed; while for N_2, because its adsorption isotherm doesn't show enough curvature, the corresponding fitting parameters exhibit high variance (**Figure S8**). We tentatively chose two cases with a low saturation capacity, n_s, and a high saturation capacity, and to see how this difference will affect the final IAST selectivity. Fitting parameters are tabulated in **Table S2**.

For adsorption in powder, as expected, the selectivity strongly depends on the fitting equation of the less-adsorbed N_2 because in this case we have to integrate the isotherm data up to an extremely high pressure [Equation S6]. When using the fitting equation with a high saturation capacity for N_2, the selectivity at 1 bar is 1637 and 1800 for 50/50 and 15/85 CO_2/N_2, respectively (**Figure S**11). If the fitting equation with a low saturation capacity is used for N_2, the selectivity will blow up and reaches $1.85*10^8$ and $2.19*10^6$ for 50/50 and 15/85 CO_2/N_2, respectively.

For adsorption in MIL-53(Al)-NH_2-200/CDA/PP case, the selectivity shows weak dependence on the different fitting equations for N_2 used. At 1 bar, MIL-53(Al)-NH_2 (200) has the highest selectivity amount three samples.

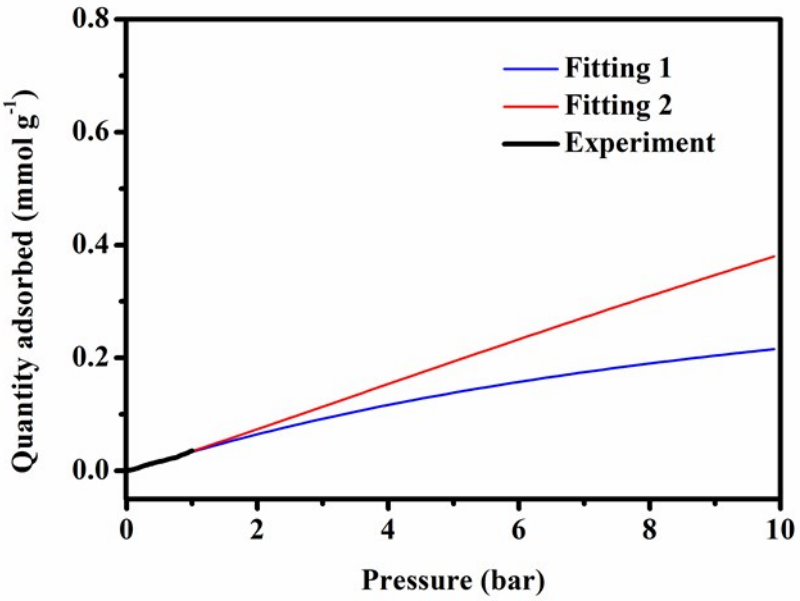

Figure S8. N_2 adsorption isotherms in MIL-53(Al)-NH_2 (powder) at 273 K.

Table S2. Fitting parameters of Sips model to pure adsorption isotherms at 273 K. For N_2 case, we chose two fitting equations that both fit experimental data well but with a low and a high saturation capacity, n_s.

Sample	Gas	n_s [mmol/g]	b [1/kPa]	n	R-square
Powder	CO_2	2.331	0.4229	1.039	0.9866
	N_2	0.4524 2.489	0.000922 0.0002161	0.9408 0.8989	0.9953 0.995
MIL-53-NH_2 (200)	CO_2	5.53	0.01368	1.012	0.9995
	N_2	3.726 9.427	0.001091 0.0004129	0.8769 0.9096	0.9998 0.9998
MIL-53-NH_2 (CDA)	CO_2	6.299	0.003601	1.305	1.0
	N_2	7.828 20.13	0.0003587 0.0001337	0.9388 0.9567	0.9986 0.9984
MIL-53-NH_2 (PP)	CO_2	3.801	7.309e-05	1.59	0.9973
	N_2	0.2742 0.8652	0.002186 0.0009088	0.7747 0.7573	0.9931 0.9959

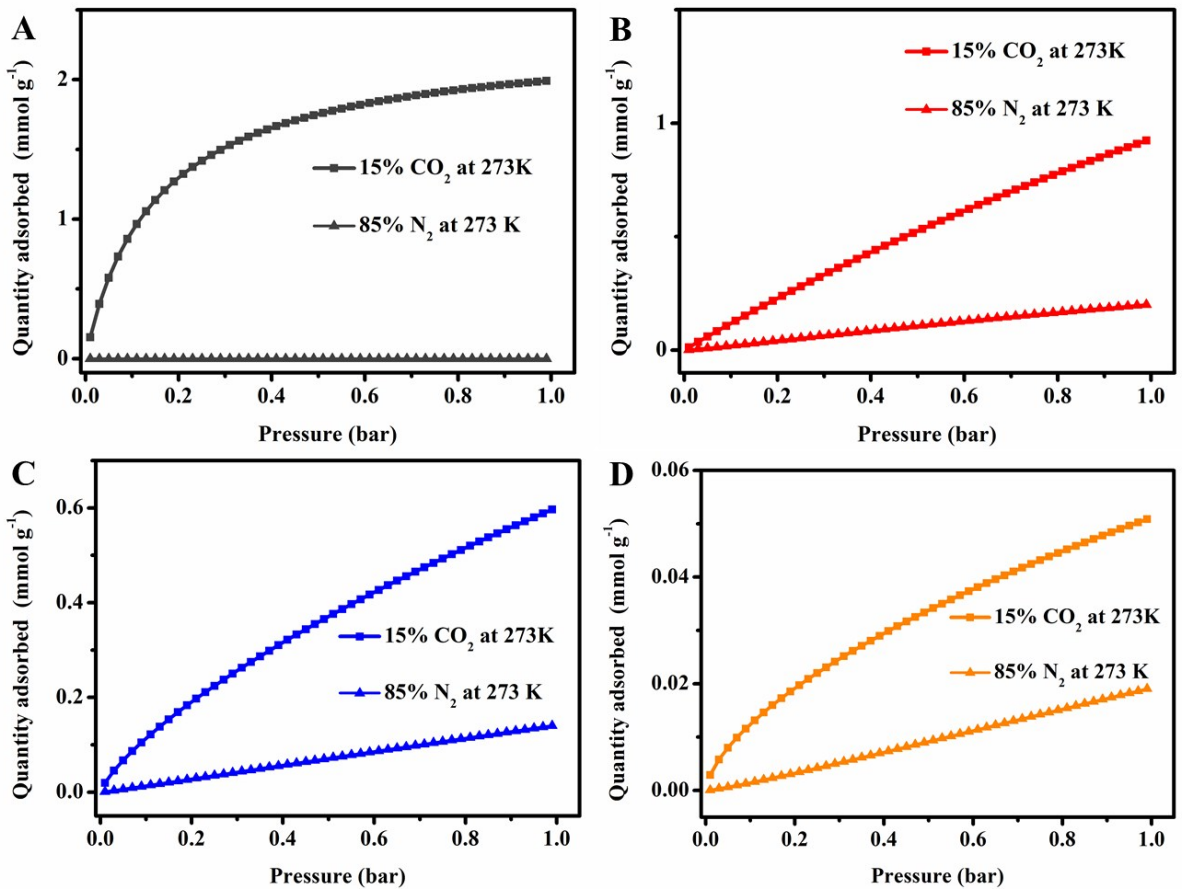

Figure S9. IAST binary adsorption isotherms for (A) MIL-53(Al)-NH_2 (powder), (B) MIL-53(Al)-NH_2 (200), (C) MIL-53(Al)-NH_2 (CDA), and (D) MIL-53(Al)-NH_2 (PP) at 273 K with CO_2 and N_2 molar ratio of 15/85 in the gas phase.

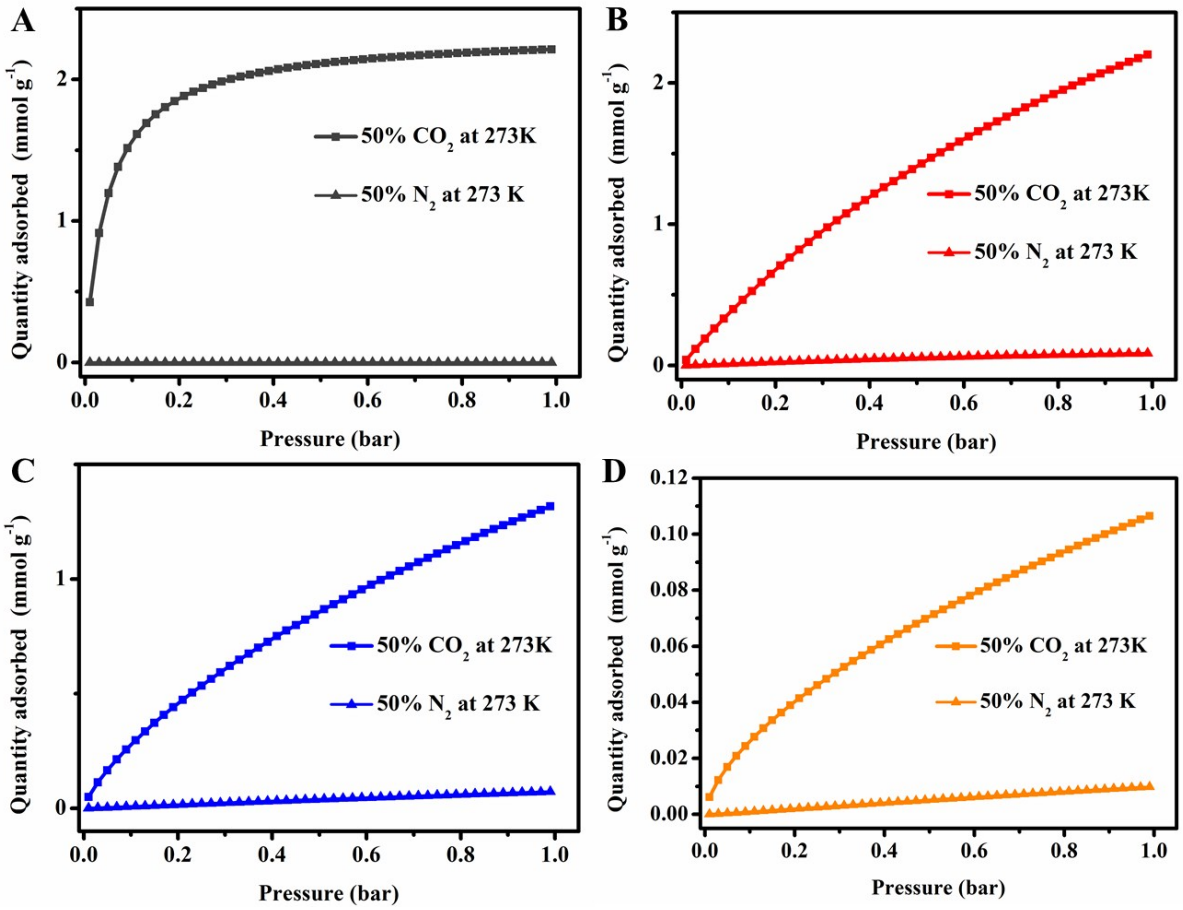

Figure S10. IAST binary adsorption isotherms for (A) MIL-53(Al)-NH_2 (powder), (B) MIL-53(Al)-NH_2 (200), (C) MIL-53(Al)-NH_2 (CDA), and (D) MIL-53(Al)-NH_2 (PP) at 273 K with CO_2 and N_2 molar ratio of 50/50 in the gas phase.

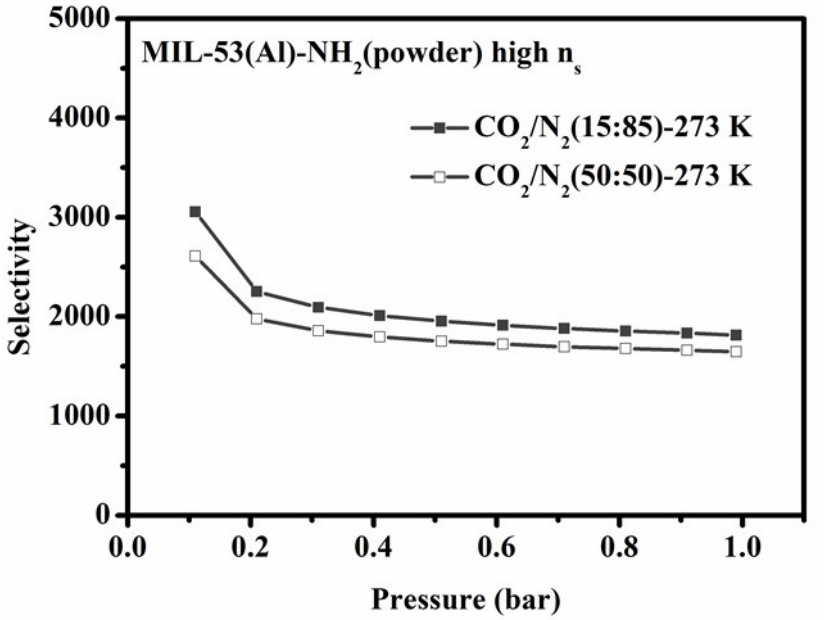

Figure S11. Selectivity by the IAST calculations for MIL-53(Al)-NH_2 (powder) at 273 K with CO_2 and N_2 molar ratio of 15/85 and 50/50 in the gas phase.

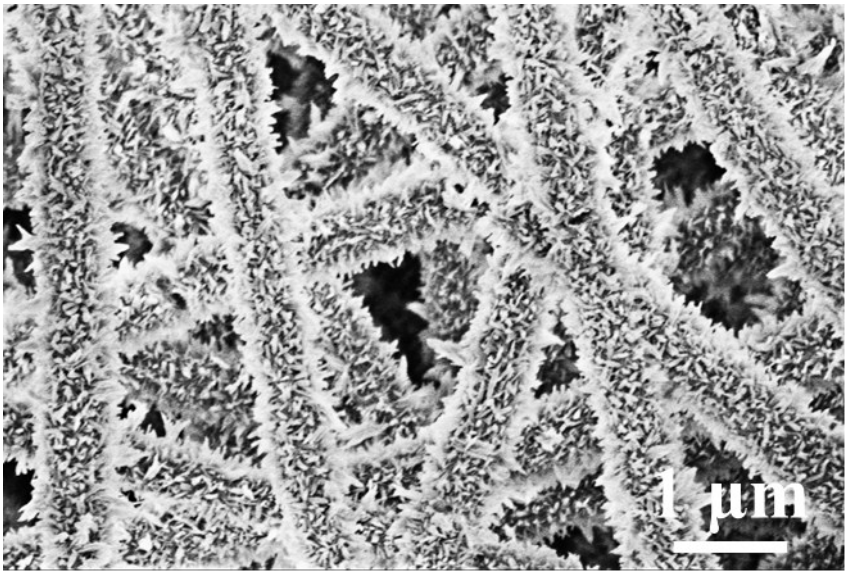

Figure S12. SEM image of MIL-53(Al)-NH_2 (200) after HCHO catalytic test.

Table S3. Summary of VOC removal performance over selected MOFs.

Material	Catalyst	VOCs	Test condition and Performance	Ref
MOF	P123/UiO-66	Toluene	Initial concentration: 1000 ppm; Adsorption capacity: 339 mg g^{-1}	15
MOF	Defective UiO-66	Toluene	Initial concentration: 1000 ppm; Adsorption capacity: 252 mg g^{-1}	16
MOF	Hydrophobic UiO-66	Toluene	Initial concentration: 1000 ppm; Adsorption capacity: 259 mg g^{-1}	17
MOF	Ga-MIL-53	Formaldehyde	Initial concentration: 2000 ppm Adsorption capacity: 70.0 mg g^{-1}	18
MOF	MOF-5	Formaldehyde	Initial concentration: 22.7 ppm Adsorption capacity: 0.11 mg g^{-1}	19
MOF	γ-CD-MOF-K	Formaldehyde	Initial concentration: 0.39 ppm Adsorption capacity: 36.7 mg g^{-1}	20
MOF	ZIF-67@PAN	Formaldehyde	Initial concentration: 0.35 ppm Removal efficiency: 84 %	21
MOF	MIL-101	Formaldehyde	Initial concentration: 150 ppm Adsorption capacity: 164.8 mg g^{-1}	22
MOF	MIL-53(Al)-NH_2 (200)	Formaldehyde	Initial concentration: 150 ppm Removal efficiency: 100 %	This work

Reference

1. J. J. Zhao, B. Gong, W. T. Nunn, P. C. Lemaire, E. C. Stevens, F. I. Sidi, P. S. Williams, C. J. Oldham, H. J. Walls, S. D. Shepherd, M. A. Browe, G. W. Peterson, M. D. Losego and G. N. Parsons, *Journal of Materials Chemistry A*, 2015, **3**, 1458-1464.
2. L. Bolinois, T. Kundu, X. R. Wang, Y. X. Wang, Z. G. Hu, K. Koh and D. Zhao, *Chemical Communications*, 2017, **53**, 8118-8121.
3. Z. J. Dai, X. W. Yu, C. Huang, M. Li, J. F. Su, Y. P. Guo, H. Xu and Q. F. Ke, *RSC Advances*, 2016, **6**, 97022-97029.
4. F. Zhang, X. Q. Zou, X. Gao, S. J. Fan, F. X. Sun, H. Ren and G. S. Zhu, *Advanced Functional Materials*, 2012, **22**, 3583-3590.
5. P. Serra-Crespo, E. Gobechiya, E. V. Ramos-Fernandez, J. Juan-Alcaniz, A. Martinez-Joaristi, E. Stavitski, C. E. A. Kirschhock, J. A. Martens, F. Kapteijn and J. Gascon, *Langmuir*, 2012, **28**, 12916-12922.
6. Z. H. Li, Y. N. Wu, J. Li, Y. M. Zhang, X. Zou and F. T. Li, *Chemistry-a European Journal*, 2015, **21**, 6913-6920.
7. H. R. Abid, Z. H. Rada, X. Duan, H. Sun and S. Wang, *Energy & Fuels*, 2018, **32**, 4502-4510.
8. A. L. Myers and J. M. Prausnitz, *Aiche Journal*, 1965, **11**, 121-+.
9. R. Sips, *Journal of Chemical Physics*, 1948, **16**, 490-495.
10. I. Langmuir, *Journal of the American Chemical Society*, 1918, **40**, 1361-1403.
11. N. Alvarez-Gutierrez, M. V. Gil, F. Rubiera and C. Pevida, *Fuel Processing Technology*, 2016, **142**, 361-369.
12. K. H. Shi, E. E. Santiso and K. E. Gubbins, *Langmuir*, 2019, **35**, 5975-5986.
13. E. Forte, A. J. Haslam, G. Jackson and E. A. Muller, *Physical Chemistry Chemical Physics*, 2014, **16**, 19165-

19180.

14. K. Sumida, D. L. Rogow, J. A. Mason, T. M. McDonald, E. D. Bloch, Z. R. Herm, T. H. Bae and J. R. Long, *Chemical Reviews*, 2012, **112**, 724-781.
15 X. D. Zhang, Y. Yang, X. T. Lv, Y. X. Wang, N. Liu, D. Chen and L. F. Cui, *Journal of Hazardous Materials*, 2019, **366**, 140-150.
16. X. D. Zhang, Y. Yang, L. Song, J. F. Chen, Y. Q. Yang and Y. X. Wang, *Journal of Hazardous Materials*, 2019, **365**, 597-605.
17. X. D. Zhang, X. T. Lv, X. Y. Shi, Y. Yang and Y. Q. Yang, *Journal of Colloid and Interface Science*, 2019, **539**, 152-160.
18. J.-P. Bellat, I. Bezverkhyy, G. Weber, S. Royer, R. Averlant, J.-M. Giraudon and J.-F. Lamonier, Journal of Hazardous Materials, 2015, **300**, 711-717.
19. Z.-Y. Gu, G. Wang and X.-P. Yan, *Analytical Chemistry*, 2010, **82**, 1365-1370.
20. L. Wang, X. Y. Liang, Z. Y. Chang, L. S. Ding, S. Zhang and B. J. Li, ACS Applied Materials & Interfaces, 2018, **10**, 42-46.
21. Y. Bian, R. T. Wang, S. J. Wang, C. Y. Yao, W. Ren, C. Chen and L. Zhang, *Journal of Materials Chemistry A*, 2018, **6**, 15807-15814.
22. Z. Wang, W. Z. Wang, D. Jiang, L. Zhang and Y. L. Zheng, *Dalton Transactions*, 2016, **45**, 11306-11311.